

Nuclear Exclusive and Semi-inclusive Measurements with a New CLAS12 Low Energy Recoil Tracker

ALERT Run Group[†]

EXECUTIVE SUMMARY

In this run group, we propose a comprehensive physics program to investigate the fundamental structure of the ^4He nucleus. An important focus of this program is the study of the partonic structure of bound nucleons. To this end, we propose next generation nuclear measurements in which low energy recoil nuclei are detected. Tagging of recoil nuclei in deep inelastic reactions is a powerful technique that will provide unique information about the nature of medium modifications, through the measurement of the EMC ratio and its dependence on the nucleon off-shellness. Other important channels are the coherent exclusive Deep Virtual Compton Scattering (DVCS) and Deep Virtual Meson Production (DVMP) with a focus on the ϕ meson. These are particularly powerful tools enabling model-independent nuclear 3D tomography through the access of partons' position in the transverse plane. These exclusive measurements will also be used to study the generalized EMC effect and for the first time access the gluonic tomography of nuclei via exclusive ϕ electroproduction channel. Finally, we propose to measure tagged DVCS on light nuclei (d, ^4He) to extract both quasi-free neutron and bound neutron and proton Generalized Parton Distributions (GPDs). In both cases, the objective is to study nuclear effects and their manifestation in GPDs including the effect of final state interactions in the measurements of the bound nucleon beam spin asymmetries and the EMC ratio.

At the heart of this program is the Low Energy Recoil Tracker (ALERT) combined with the CLAS12 detector. The ALERT detector is composed of a stereo drift chamber for track reconstruction and an array of scintillators for particle identification. Coupling these two types of fast detectors will allow ALERT to be included in the trigger for efficient background rejection, while keeping the material budget as low as possible for low energy particle

[†]Contact Person: Kawtar Hafidi (kawtar@anl.gov)

detection. ALERT will be installed inside the solenoid magnet instead of the CLAS12 Silicon Vertex Tracker. We will use an 11 GeV longitudinally polarized electron beam (80% polarization) of 150 nA on a gas target straw filled with deuterium or ^4He at 3 atm to obtain a luminosity of $3.10^{34} \text{ cm}^{-2}\text{s}^{-1}$. In addition we will need to run hydrogen and ^4He targets at different beam energies for detector calibration. The following table summarizes our beam time request:

Measurements	Particles detected	Targets	Beam time request	Luminosity*
ALERT Commissioning	p, d, ^4He	H and He	5 days	Various
Tagged EMC	p, ^3H , ^3He	^2H and He	20 + 20 days	$3.10^{34} \text{ cm}^{-2}\text{s}^{-1}$
Tagged DVCS	p, ^3H , ^3He	^2H and He	20 + 20 days	$3.10^{34} \text{ cm}^{-2}\text{s}^{-1}$
Nuclear GPDs	^4He	He	extra 10 days on He	$6.10^{34} \text{ cm}^{-2}\text{s}^{-1}$
Additional Topics	p, d, ^3H , ^3He	^2H and He	20 + 20 + (10) days	$3(6).10^{34} \text{ cm}^{-2}\text{s}^{-1}$
TOTAL			55 days	

*This luminosity value is based on the effective part of the target. When accounting for the target's windows, which are outside of the ALERT detector, it is increased by 60%

Tagged Deeply Virtual Compton Scattering Off Light Nuclei

W.R. Armstrong[‡], J. Arrington, I. Cloet, K. Hafidi[†], M. Hattawy, D. Potterveld,
P. Reimer, Z. Yi

Argonne National Laboratory, Lemont, IL 60439, USA

J. Ball, M. Defurne, M. Garçon, H. Moutarde, S. Procureur, F. Sabatié
CEA, Centre de Saclay, Irfu/Service de Physique Nucléaire, 91191 Gif-sur-Yvette, France

W. Cosyn

*Department of Physics and Astronomy, Proeftuinstraat 86, Ghent University, 9000 Ghent,
Belgium*

M. Mazouz

Faculté des Sciences de Monastir, 5000 Tunisia

A. Accardi

Hampton University, Hampton, VA 23668, USA

J. Bettane, G. Charles, R. Dupré[†], M. Guidal, D. Marchand, C. Muñoz, S. Niccolai,
E. Voutier

*Institut de Physique Nucléaire, CNRS-IN2P3, Univ. Paris-Sud, Université Paris-Saclay,
91406 Orsay Cedex, France*

K. P. Adhikari, J. A. Dunne, D. Dutta, L. El Fassi, L. Ye

Mississippi State University, Mississippi State, MS 39762, USA

M. Amarian, G. Dodge

Old Dominion University, Norfolk, VA 23529, USA

V. Guzey

[‡]Contact person

[†]Spokesperson

*Petersburg Nuclear Physics Institute, National Research Center "Kurchatov Institute",
Gatchina, 188300, Russia*

N. Baltzell, S. Stepanyan

Thomas Jefferson National Accelerator Facility, Newport News, VA 23606, USA

S. Joosten, Z. E. Meziani[†], M. Paolone

Temple University, Philadelphia, PA 19122, USA

F. Cao, K. Joo, A. Kim, N. Markov

University of Connecticut, Storrs, CT 06269, USA

S. Scopetta

Università di Perugia, INFN, Italy

W. Brooks, A. El-Alaoui

Universidad Técnica Federico Santa María, Valparaíso, Chile

S. Liuti

University of Virginia, Charlottesville, VA 22903, USA

a CLAS Collaboration Proposal

Abstract

Deeply Virtual Compton Scattering (DVCS) on the proton is set to reveal a 3 dimensional picture of how quarks and gluons are distributed inside the nucleon. Incoherent DVCS, i.e., DVCS on a nucleon contained inside a nucleus, can in principle be used to study the 3D tomography of a bound nucleon relative to a free one. However, the unknown Fermi motion of the struck nucleon and final state interactions complicate identifying any deviations from the free nucleon case as originating from modifications at the partonic level. Through spectator tagging, where the target nucleus (A) has one nucleon removed through DVCS and a recoiling spectator system (A-1) is detected, the initial momentum of the active nucleon can be determined in the impulse approximation. Probing relatively large initial nucleon momentum (relative to Fermi momentum) provides an interesting opportunity to study mean field effects and short range correlations. The latter corresponds to configuration where two nucleons are separated by a small distance. On the other hand, probing smaller initial nucleon momentum in ^4He is more sensitive to the mean field potential given the binding per nucleon of 20 MeV compared to the case of deuterium where it is of 2.2 MeV. That explains the fact that deuterium is often used to study properties of the neutron. In order to unambiguously identify mean field modified nucleons, final state and short range correlations for small initial momenta of the nucleus need to be separated. This experiment is designed to specifically address issues of final state interactions, Fermi motion and short range correlations for incoherent DVCS.

We propose measuring these effects through DVCS on ^4He and deuterium targets, where the measured final state includes the recoiling nucleus (A-1) and the struck nucleon. Under these conditions, the incoherent DVCS processes offers a rare ability to simultaneously quantify final state interactions, measure initial nucleon momentum, and provide a sensitive probe to other nuclear effects at the parton level. The DVCS beam spin asymmetry on a (quasi-free) neutron will be measured through tagging a recoil proton from a deuteron target. Similarly, a bound neutron measurement will be performed by detecting a recoiling ^3He when scattering off ^4He target. These two observables will allow for a self-contained measurement of nuclear modifications to the neutron, known as the “off-forward EMC Effect”, while additionally providing a clean neutron DVCS measurement with a technique similar to the one used in BoNuS experiments.

We will also measure the impact of final state interactions on incoherent DVCS when the scattered electron, the real photon, and the struck proton are detected in the final state. This will help understand the measurements performed on helium during the previous CLAS E-08-024 experiment and will allow better measurements of the same channel where both statistics and kinematical coverage are extended. The measurement of neutron DVCS by tagging the recoil proton from a deuterium target is complementary to the previously approved CLAS12 experiment E12-11-003 which will also measure quasi-free neutron DVCS by detecting the scattered neutron.

Contents

Abstract	5
Introduction	8
1 Physics Motivations	11
1.1 Nuclear Effects	11
1.1.1 The EMC Legacy	11
1.1.2 Measuring Medium Modified Nucleons	12
1.1.3 Why <i>Tagged</i> DVCS?	12
1.2 Generalized Parton Distributions	14
1.2.1 Spin Sum Rule	14
1.2.2 Polarized EMC Effect	15
1.2.3 Models of Nuclear Effects	16
1.3 Motivation Summary	19
2 Formalism and Experimental Observables	20
2.1 Deeply Virtual Compton Scattering	20
2.1.1 DVCS Beam Spin Asymmetry	22
2.2 Tagged DVCS Reactions	23
2.2.1 n-DVCS with a ^2H Target	23
2.2.2 n-DVCS and p-DVCS with a ^4He Target	24
3 Experimental Setup	27
3.1 The CLAS12 Forward Detector	27
3.2 Design of the ALERT Detector	29
3.2.1 The Drift Chamber	30
3.2.2 The scintillator array	33
3.3 Reconstruction	36
3.3.1 Track Fitting	37
3.3.2 Track Reconstruction and Particle Identification	38
3.4 Drift chamber prototype	41
3.5 Other options for a Low Energy Recoil Detector	42

3.5.1	Central Detector	43
3.5.2	BoNuS12 Radial Time Projection Chamber	44
3.5.3	Summary	45
3.6	Technical contributions from the research groups	46
3.6.1	Argonne National Laboratory and Temple University	46
3.6.2	Institut de Physique Nucléaire d'Orsay	46
3.6.3	Jefferson Laboratory	47
4	Proposed Measurements	48
4.1	Asymmetry Extraction Procedure	48
4.2	Kinematic Coverage	49
4.3	Projections	51
4.3.1	Beam Spin Asymmetry Extraction	51
4.3.2	Systematic Uncertainties	56
	Summary and Beam Time Request	61
A	DVCS Formalism	68
A.1	Theory bound nucleon DVCS	68
B	Detailed Experimental Projections	75
B.1	Kinematic Coverage	75
B.2	Projections for $\sin \phi$ harmonic of the BSA	79
B.2.1	Off-forward EMC Effect Ratio	82

Introduction

Deeply virtual Compton scattering is widely used to extract information about the generalized parton distributions (GPDs) of the nucleon. Its usefulness comes from the fact that the final state photon does not interact strongly (at leading order), requiring no additional non-perturbative formation mechanism. That is, the process in which the active quark radiates a final state photon is well understood, therefore, it is very useful for extracting information about the unknown non-perturbative blob shown in Fig. 1.

The extracted GPDs offer a three dimensional picture of how quarks and gluons are distributed in the nucleon. DVCS measurements on the proton [1, 2, 3, 4] and neutron [5] have already begun to provide insight into this slowly developing picture of the nucleon, however, without a free neutron target a flavor separation will always require using a quasi-free neutron target bound in light nuclei such as deuterium or ^3He . Such an extraction requires control of numerous nuclear effects: Fermi motion, off-shellness of the nucleons, mean field modified nucleons, short-range correlations (SRC), and final-state interactions (FSI)

Most observables involving nuclear targets (*e.g.*, inclusive DIS, tagged DIS, inclusive quasi-elastic, semi-inclusive nucleon knockout, and polarization transfer in quasi-elastic scattering) are sensitive to many of these nuclear effects. Some experiments have been conducted in such a way as to mitigate or provide some systematic control over the size of these effects [6, 7, 8]. However, as discussed in the next chapter, the very nature of each experiment often precludes control of one or more nuclear effect mentioned above. Therefore, it is difficult to unambiguously draw conclusions from these measurements as to whether a nucleon is modified in a nuclear environment.

Much like the DVCS observables' ability to cleanly access information about the GPDs, tagged incoherent DVCS analogously provides a method for cleanly extracting nuclear effects from the observables. In a fully exclusive reaction, the over determined kinematics yield two measurements of the same momentum transfer (see Fig. 1). Within the plane wave Born approximation (PWBA), the momentum transfer between the virtual and real photon is completely insensitive to FSI. On the other side of the diagram, the momentum transfer calculated between the initial and final nucleon is quite sensitive to FSI under the assumption

that the plane wave impulse approximation (PWIA) holds. That is to say, any relative deviation between the two momentum transfers can be attributed to the breakdown of the PWIA. In this way we can identify the kinematics where FSI are significant and where they are minimal. Unlike, fully exclusive quasi elastic knockout reactions, tagged DVCS has a unique opportunity to simultaneously probe nuclear effects at the parton level.

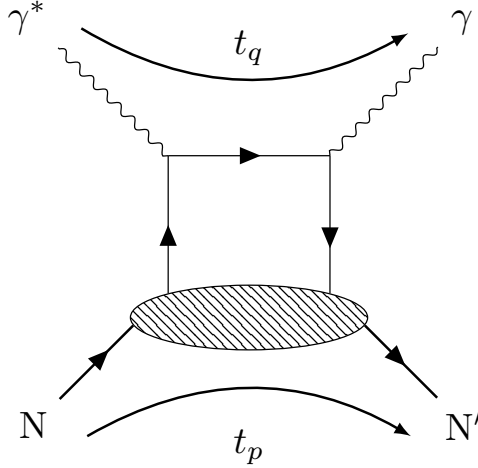


Figure 1: The DVCS handbag diagram showing the two ways the momentum transfer can be calculated.

Therefore, we propose to measure tagged DVCS beam spin asymmetries (BSA) on two nuclear targets (^2H and ^4He) to unambiguously determine if the nucleon is modified in a nuclear environment. We will measure three beam spin asymmetries through tagged incoherent DVCS using two gas targets. The experiment requires the measurement of the three main processes:

1. $^4\text{He} + \gamma^* \rightarrow \gamma + p + ^3\text{H}$
2. $^4\text{He} + \gamma^* \rightarrow \gamma + (n) + ^3\text{He}$
3. $^2\text{H} + \gamma^* \rightarrow \gamma + (n) + p$.

The first process provides a measurement of bound proton DVCS, but more importantly, by also detecting the final state proton, provides the over-determined kinematics needed to systematically probe the size of FSI. This measurement is of critical importance to unwinding the nuclear effects when analyzing the last two processes, bound and quasi-free neutron DVCS, where the active nucleon (a neutron) goes undetected. A self-contained analysis of the nuclear effects on a neutron will be compared to a similar analysis of the proton. That latter will use the measured bound proton results along with the previously measured results or already approved free proton DVCS [9, 10] experiments. In this way we will extract for the proton and the neutron an “off-forward EMC effect”, *i.e.*, the ratio of a bound nucleon’s off-forward structure function in ^4He to a free nucleon’s off-forward structure function.

A large acceptance detector system capable of running at high luminosity along with the ability to detect or “tag” the low energy recoil spectator system is needed to perform such measurements. Clearly, CLAS12 is the ideal choice for this experiment augmented by *a low energy recoil tracker* (ALERT) which cleanly identifies the recoiling spectator system down to the lowest possible momentum. The ALERT detector consists of a small drift chamber that is insensitive to minimum ionizing particles, and a surrounding scintillator hodoscope that principally provides TOF information.

The outline of this proposal is as follows. Chapter one will provide a detailed motivation for the experiment. Chapter two will present the formalism and the observables we aim to measure. Chapter three presents a discussion of detector requirements, specifically, the detectors of CLAS12 and the need for a new low energy recoil recoil detector. Chapter four will discuss the experimental deliverables, kinematic coverage, projected results, and required beam time for the proposed experiment.

Chapter 1

Physics Motivations

Before diving into the details of tagged incoherent DVCS, we will first explain why an understanding of the nature and origins of nuclear effects is important for determining the nucleon structure at the parton level. We will begin this chapter with a discussion of nuclear effects and the challenges they present to experiment. This is followed by a quick overview of GPDs and their importance to understanding the partonic structure of nuclear matter. The kinematics of incoherent DVCS are discussed, highlighting the critical importance of the spectator tagging method. We will emphasize the unique opportunity tagged DVCS has to finally settle the more than three decades old question: *is the partonic structure of the nucleon modified in presence of a nuclear medium?*

1.1 Nuclear Effects

1.1.1 The EMC Legacy

Measurements of the longitudinal parton distribution functions (PDFs) with polarized beams and targets have provided a detailed one dimensional mapping of the quark distributions in the nucleon. QCD has been successful in describing the evolution of these distributions across scales differing by many orders of magnitude. The European Muon Collaboration (EMC) not only observed the so-called “EMC effect”, but they also created the poorly named “spin crisis”. The EMC effect originates from their observation that the naive expectation of the quark distributions in nuclei, *i.e.*, they are the sum of the quark distributions for A free nucleons, was not observed [11]. However, consensus has yet to be reached in how to explain this effect. The spin crisis began when it was discovered that the spin of the quarks only carry a small fraction of the nucleon’s total spin. It was soon understood that, through the non-perturbative dynamics of QCD, the remaining angular momentum will likely come in the form of quark orbital angular momentum (OAM) and gluon angular momentum. The EMC experiments gave us a “crisis” that was quickly understood, and an empirical “effect”

whose origins remain ambiguous more than 3 decades later.¹

1.1.2 Measuring Medium Modified Nucleons

The EMC effect showed the possibility of medium modifications to the nucleon may be significant in deep inelastic scattering². However, the degree to which these modifications can be cleanly studied in inclusive or semi-inclusive processes is made difficult by the possible presence of final state interactions (FSI). Furthermore, when considering the Fermi motion of a bound nucleon, there exists a probability of finding a nucleon moving with large relative momenta which corresponds to a configuration where the two nucleons are separated by a small distance. By selecting these dense configurations through spectator tagging in hard processes, it is not unreasonable to expect sizable modifications relative to the mean field nucleons [12]. Therefore, knowing precisely the initial momentum of the struck nucleon is key to understanding the short and long range nuclear effects. Isolating the configuration space effects from the FSIs presents a significant obstacle to drawing a definitive conclusion about medium modifications.

Similar medium modifications are expected to manifest themselves in the elastic form factors of bound nucleons. Observation of saturation of the Coulomb sum rule (CSR), which is accessible through measurements of the longitudinal response function in quasi-elastic scattering off nuclei, has been debated for some time [13, 14]. An observed quenching of the sum rule would indicate that nucleons are modified in such a way that the net charge response of the parent nucleus is much more complicated than a simple sum of nucleons. Recent, QCD inspired theoretical work predicts a dramatic quenching of the sum rule [15]. Furthermore, observations of short range correlated nucleon pairs in knockout reactions have challenged us to confront our ignorance of the short-range part of the N-N potential.

While a consensus has yet to be reached in explaining the origins of and the connections between the EMC effect, short range correlations, and quenching of the Coulomb sum rule, medium modifications of the nucleon is expected to play an important role in these phenomena.

1.1.3 Why *Tagged* DVCS?

DVCS is poised to provide some much needed contact between the EMC effect and short-range correlations. The two phenomena are observed through notably different processes but the connection between the inelastic and elastic observables is due to the properties of GPDs (see A.1). In the forward limit the GPDs reduce to the longitudinal

¹In hindsight, perhaps the “EMC effect” should have been called the “EMC Crisis”, and the “spin crisis” called the “EMC spin effect”.

²Perhaps the earliest known medium modification of the nucleon is the free neutron lifetime compared to the significantly longer lifetime when bound in a nucleus.

parton distributions whose modification may explain the EMC effect, and in the off-forward case they reduce to the form factors, thus, describing elastic scattering off of the nucleon. Therefore, measurements of nucleon GPDs in nuclei will bridge the gap between these two processes and will shed light on the connections between the EMC effect and short range correlations. The sensitivity of the GPDs to medium modifications is a significant motivation, however, *tagged* incoherent DVCS provides an unprecedented handle on quantifying and systematically controlling the various nuclear effects.

First consider the inclusive DIS measurements where only the scattered electron is detected and the exchanged virtual photon interacts at the parton level. The nucleon containing the struck quark may potentially be in a short-range correlated N-N pair, therefore, tagging the spectator system in the PWIA provides the experimental handle needed to compare the contributions to the EMC effect from SRC nucleons versus the nucleons in the mean field. This measurement is part of the “Tagged EMC” proposal found in the current proposal’s run group. Here, FSIs are the principle challenge for this method which become amplified at larger initial nucleon momentum. The re-interaction of the spectator system (A-1) with hadronizing fragments (X) can alter the detected momentum of the spectator system. Therefore model calculations have to be used to explore kinematics where FSI can be minimized [16].

Similarly, for inclusive quasi-elastic scattering we would like to measure the nucleon elastic form factor modifications associated with the SRC and the mean-field nucleons. Therefore, by detecting the knockout nucleon or a spectator recoil, the initial nucleon’s momentum can be determined (within the PWIA). If both are detected, the overdetermined kinematics allow for a second calculation of the momentum transfer. However, for large nuclei the possibility of detecting the full (A-1) recoil system becomes nearly impossible. Furthermore, FSI in the form of meson exchange currents (MEC) can become rather troublesome even for measurements of induced polarization in quasi-elastic knock-out reactions. Therefore, again, we find an explicit model dependence spoiling the interpretation of medium modifications.

Finally, incoherent DVCS has a unique combination characteristics found in DIS and quasi-elastic scattering that make it the ideal process for exploring nuclear effects. Like both processes, tagging the recoil spectator system serves to identify and separate the mean field (low momentum) nucleons from the SRC (high momentum) nucleons. Similar to DIS, DVCS has a parton level interpretation, and like elastic scattering the process is exclusive. The latter property allows for systematic control of the FSIs through the redundant measurement of the momentum transfer, t . Therefore, tagged incoherent DVCS provides a *model independent* method for studying and accounting for final state interactions while providing an observable that is uniquely sensitive to the medium modifications.

1.2 Generalized Parton Distributions

1.2.1 Spin Sum Rule

By studying the “off-forward parton distributions”, Ji derived a sum rule [17] which is a gauge invariant decomposition of the nucleon spin. It relates integrals of the GPDs to the quark total angular momentum and is written as

$$J_q = \frac{1}{2} \int dx x [H_q(x, \xi, t = 0; Q^2) + E_q(x, \xi, t = 0; Q^2)] \quad (1.1)$$

where the H_q and E_q are the leading-twist chiral-even quark GPDs. An identical expression for the total gluon orbital angular momentum is obtained using the two gluon GPDs, H_g and E_g . The total nucleon spin is simply written as

$$\frac{1}{2} = \sum_q J_q + J_g \quad (1.2)$$

where the sum is over light quark and anti-quarks. A topic of heavy discussion over the past five years or so has been about the decomposition of the nucleon spin. Ji showed that the gluon angular momentum cannot be broken into spin and orbital in a gauge invariant way, however, the quark can. In fact, the polarized PDFs provide the quark spin contribution in the forward limit

$$\Delta\Sigma_q(Q^2) = \int dx x \tilde{H}_q(x, \xi = 0, t = 0; Q^2) \quad (1.3)$$

where $\Delta\Sigma_q$ is the integral of the polarized PDF Δq . Therefore, we arrive at an expression for the quark OAM

$$L_q = J_q - \frac{1}{2} \Delta\Sigma_q \quad (1.4)$$

which, through equations 1.1 and 1.3, is a function of the quark GPDs E , H , and \tilde{H} .

The GPDs of the up and down quarks can be extracted from measurements on the neutron and proton using isospin symmetry

$$F_u = \frac{3}{5} (4F^p - F^n) \quad (1.5)$$

$$F_d = \frac{3}{5} (4F^n - F^p) \quad (1.6)$$

where $F \in [H, E, \tilde{H}, \tilde{E}]$. The flavor separation is straight forward if equal data on the proton and neutron GPDs are available. However, clean neutron data is not available due to a non-existent free-neutron target, and when neutron measurements are made using nuclear targets they suffer from a variety of nuclear effects previously discussed. Part of the proposed

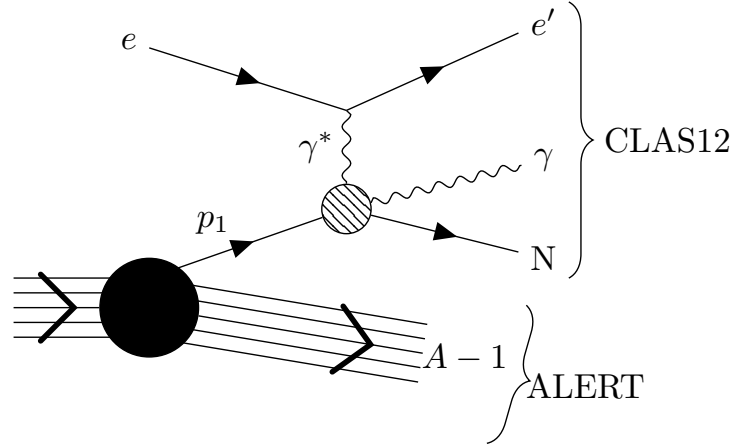


Figure 1.1: Tagged DVCS diagram showing the detection of the forward DVCS final state particles in CLAS12 and the detection of the recoiling spectator system (A-1) in ALERT. The hatched circle represents the hard DVCS process.

experiment would provide a precise neutron measurement from deuteron with a technique similar to the one used by BoNuS to extract the neutron structure function as high x [18, 19].

1.2.2 Polarized EMC Effect

Using polarized nuclear targets, the polarized EMC effect can be measured and is predicted to be larger than the “unpolarized” EMC effect [20]. The polarized EMC effect is measured through the ratio of spin structure functions g_1 of a bound nucleon to that of a free nucleon. DIS measurements typically require both a longitudinally polarized target and longitudinally polarized beam to measure g_1 . The $\sin \phi$ harmonic of the neutron DVCS beam spin asymmetry is

$$A_{LU,n}^{\sin \phi} \propto \text{Im}(F_1^n \mathcal{H}^n - \frac{t}{4M^2} F_2^n \mathcal{E}^n + \frac{x_B}{2} (F_1 + F_2)^n \tilde{\mathcal{H}}^n) . \quad (1.7)$$

The first term is suppressed by F_1^n and if for the moment we neglect the \mathcal{E} term, the ratio of this asymmetry for a bound neutron to a free neutron is

$$R_{AL,n}^{\sin \phi} = \frac{A_{LU,n^*}^{\sin \phi}}{A_{LU,n}^{\sin \phi}} \simeq \frac{G_M^{n^*}(t) \text{Im}(\tilde{\mathcal{H}}^{n^*}(\xi, \xi, t))}{G_M^n(t) \text{Im}(\tilde{\mathcal{H}}^n(\xi, \xi, t))} \quad (1.8)$$

which in the forward limit becomes

$$R_{AL,n}^{\sin \phi} \longrightarrow \frac{\mu_{n^*}}{\mu_n} \frac{g_1^{n^*}(x)}{g_1^n(x)} , \quad (1.9)$$

where μ_{n^*}/μ_n is the ratio of the bound neutron magnetic moment to the free neutron magnetic moment, and $g_1^{n^*}/g_1^n$ is similarly the ratio of the bound to free neutron spin structure functions.

Equations 1.8 and 1.9 are rather interesting for a few reasons. First, they can be used to draw conclusions about the behavior of the *polarized* quark distributions in unpolarized nuclei without using a polarized target. But we must note the unjustified neglect of the \mathcal{E}^n term which complicates subsequent analysis. We point out this term in the ratio of Equation 1.8 because it highlights the observable's sensitivity to medium modifications. Specifically noting that a modification to the nucleon's static properties, such as, anomalous magnetic moment or polarization-dependent transverse-charge distribution (see [21]), would also manifest themselves through the magnetic form factor whose ratio also appears in this observable.

Also, a measurement of the BSA in Equation 1.7 will provide important model constraints on the GPD E^n and measurements of the ratio with ^4He would further constrain nuclear GPD models. This is particularly motivating in the context of Equation 1.1, where E^n is clearly an important quantity for understanding the quark orbital angular momentum.

1.2.3 Models of Nuclear Effects

To understand the potential sources of observable nuclear effects, we take the ratio of beam spin asymmetries for a bound nucleon to that on the free nucleon target. Here we discuss just two models that make very different predictions for similar ratios based on the presumed sources of the nuclear effects.

First, predictions for the ratio of beam spin asymmetry at 6 GeV are shown in Fig. 1.2, which shows the bound proton beam spin asymmetry, $A_{LU}^{p^*}$, to the free proton A_{LU}^p [22]. These calculations use the medium modified GPDs as calculated from the quark-Meson coupling model. However, they do not include FSIs and predict their contribution is at most a few percent. In another calculation, Liuti, et. al. [23, 24] use a realistic spectral function and consider off-shell effects. This is a more traditional approach to explaining differences in a bound nucleon. They make predictions for the ratio

$$R_A(x, \xi = 0, t) = \frac{H_A(x, \xi = 0, t)F_N(t)}{H_N(x, \xi = 0, t)F_A(t)} \quad (1.10)$$

which is shown in Fig. 1.3. For more discussions of modeling nuclear effects see [25, 26].

It is clear that the role of off-shellness, and final state interactions in nuclei needs to be better understood if we are to conclude that the nucleon structure is modified by the nuclear medium. With spectator tagging, we will be able to test these models over a broad range of spectator momentum and angles. This tagging technique can be used a knob to tune the effect of final state interactions and either maximized or minimized it.

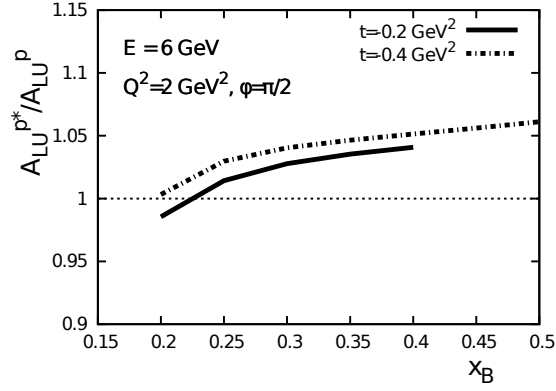


Figure 1.2: Beam spin asymmetry ratio of a bound proton to a free proton. Reproduced from [22].

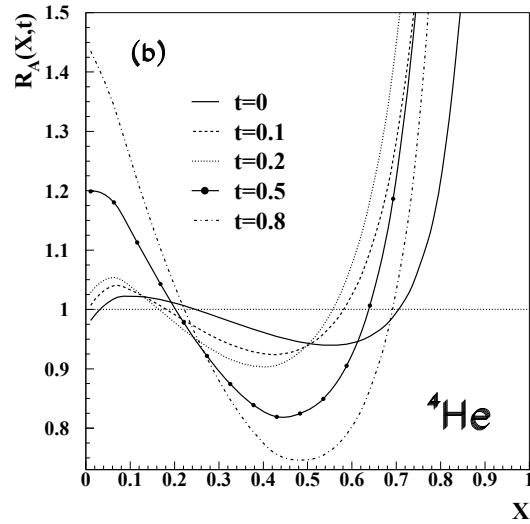


Figure 1.3: Predictions for the ratio given in equation 1.10. Reproduced from [23].

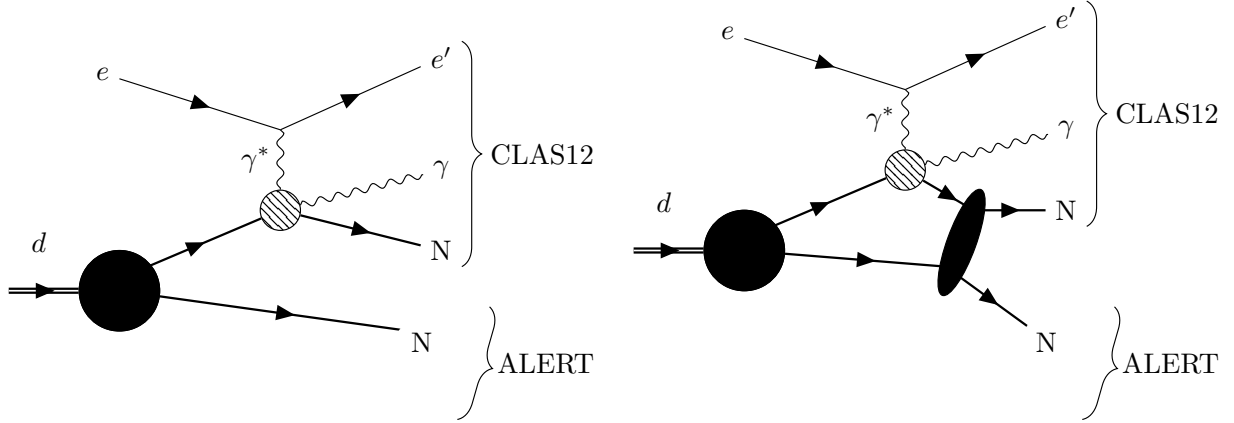


Figure 1.4: PWIA diagram for incoherent DVCS on the deuteron (left) and with the inclusion of final state interactions (right).

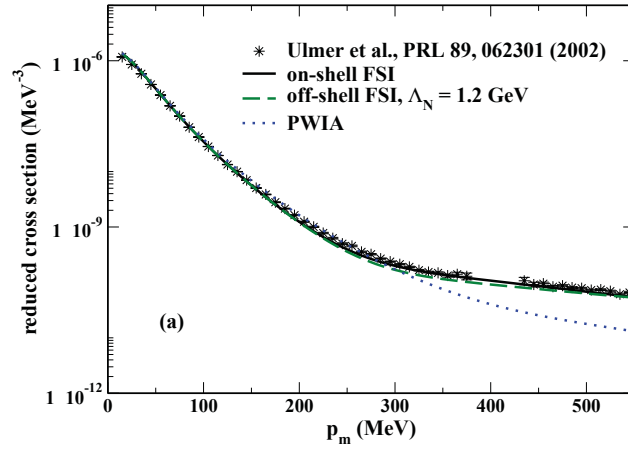


Figure 1.5: Reduced quasi-elastic scattering cross section on deuteron. Reproduced from [27].

To understand the regions where FSI are expected to be significant, we first look at the deuteron. Consider the quasi-elastic scattering on a quasi-free nucleon as shown in Fig. 1.4. Measurements of the cross section as a function of missing momentum are shown in Fig. 1.5 along with model calculations in PWIA with different final state interactions. From model calculations it was found that the PWIA was insufficient for describing the data at missing momenta above 300 MeV/c. Similarly, the size of the FSI effects as a function of spectator momentum (left) and angle relative to the momentum transfer, θ_s , (right) is shown in Fig. 1.6 [16]. At low recoil momentum and backwards spectator angle, the FSI are negligible, where at high momenta perpendicular to the momentum transfer, the FSI are maximized.

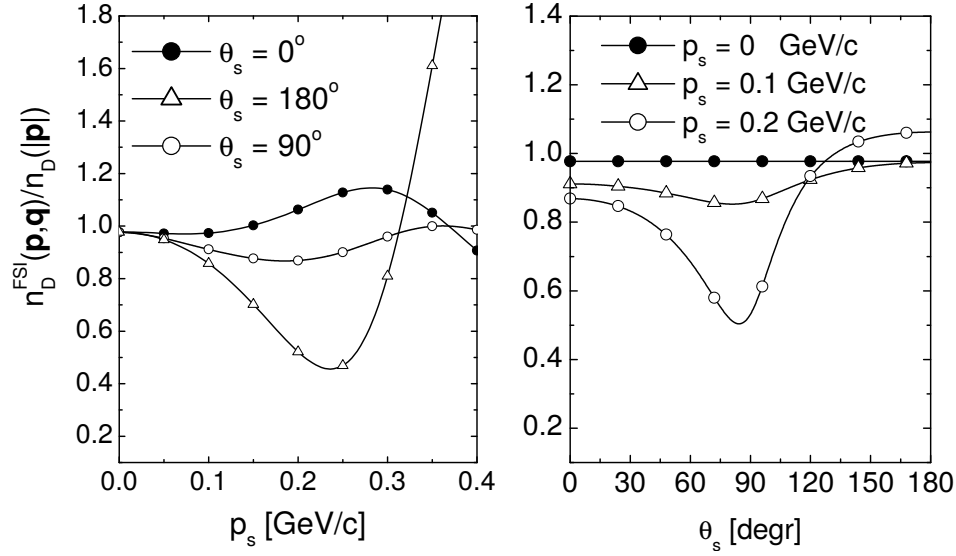


Figure 1.6: Ratio of cross sections for the FSI model from [16] to PWIA calculation as a function of the spectator momentum (left) and spectator angle (right).

1.3 Motivation Summary

In summary, we propose to perform the following key measurements using CLAS12 and ALERT for the low energy spectator recoil tagging:

- *Bound proton DVCS* with a ^4He target where the final state is fully detected by tagging a spectator ^3H and the struck proton is detected in CLAS12. The PWIA will be tested by the redundant measurement of the momentum transfer as explained above. Thus, FSI-free kinematics are identified in a completely *model independent* way.
- *Bound neutron DVCS* with a ^4He target where the neutron goes undetected and the spectator ^3He is detected in ALERT. Using the FSI-free kinematics identified with the previous measurement, and using iso-spin (charge) symmetry, we will conclude that the struck neutron was equally free of final state interactions.
- *Quasi-free neutron DVCS* with a ^2H target where the recoil proton is tagged and the struck neutron goes undetected.

Chapter 2

Formalism and Experimental Observables

2.1 Deeply Virtual Compton Scattering

The cross section for DVCS on a spin-1/2 target can be parameterized in terms of four helicity conserving GPDs: H^q , E^q , \tilde{H}^q , and \tilde{E}^q . For spin-0 targets, such as ^4He , the cross section is parameterized with just one helicity conserving GPD [28]. For spin-1 targets like the deuteron, the cross section is parameterized with nine GPDs [29, 30]. The DVCS cross section is written as

$$\frac{d\sigma}{dx_A dy dt d\phi d\varphi} = \frac{\alpha^3 x_A y}{16\pi^2 Q^2 \sqrt{1 + \varepsilon^2}} \left| \frac{\mathcal{T}}{e^3} \right|^2 \quad (2.1)$$

where

$$\varepsilon \equiv 2x_A \frac{M_A}{Q}, \quad (2.2)$$

$x_A = Q^2/(2p_1 \cdot q_1)$ is the scaling variable, $y = (p_1 \cdot q_1)/(p_1 \cdot k_1)$ is the photon energy fraction, ϕ is the angle between the leptonic and hadronic planes, φ , is the electron's azimuthal angle, $Q^2 = -q_1^2$, and $q_1 = k_1 - k_2$. The particle momentum definitions are shown in Fig. 2.1. We use the BMJ convention [31, 32, 33, 34] for defining the momentum transfer where the target nucleus is initially at rest, $\Delta = p_1 - p_2$ and $t = \Delta^2$. The Bjorken variable is related to the scaling variable by

$$x_B = \frac{Q^2}{2M_N E y} \simeq A x_A \quad (2.3)$$

where M_N is the nucleon mass and E is the beam energy. Another scaling variable called skewedness is

$$\xi = \frac{x_A}{2 - x_A} + \mathcal{O}(1/Q^2) \quad (2.4)$$

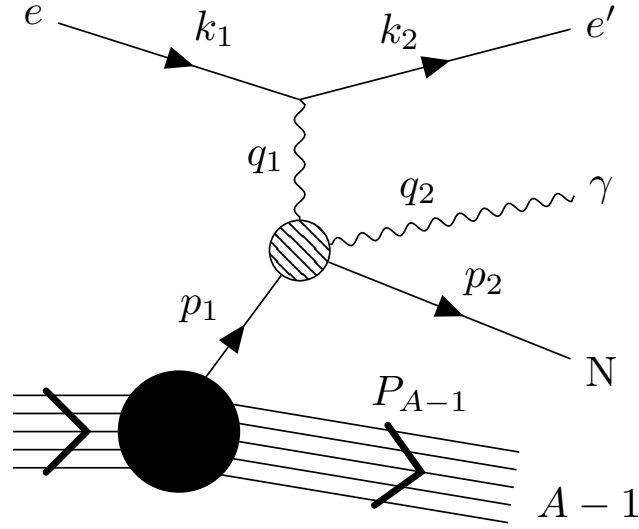


Figure 2.1: Incoherent DVCS process with the momentum definitions labeled.

where the power suppressed contributions originate with the selection of the BMJ frame convention needed to unambiguously define the leading-twist approximation used in this proposal [31].

The amplitude is the sum of the DVCS and Bethe-Heitler (BH) amplitudes, and when squared has terms

$$\mathcal{T}^2 = |\mathcal{T}_{\text{BH}}|^2 + |\mathcal{T}_{\text{DVCS}}|^2 + \mathcal{I} \quad (2.5)$$

where the first is the BH contribution, the second is the DVCS part, and the last term is the interference part,

$$\mathcal{I} = \mathcal{T}_{\text{DVCS}} \mathcal{T}_{\text{BH}}^* + \mathcal{T}_{\text{DVCS}}^* \mathcal{T}_{\text{BH}}. \quad (2.6)$$

The corresponding amplitudes are calculated with the diagrams shown in Fig. 2.2. The details of contracting the DVCS tensor with various currents and tensors can be found in [30]. The

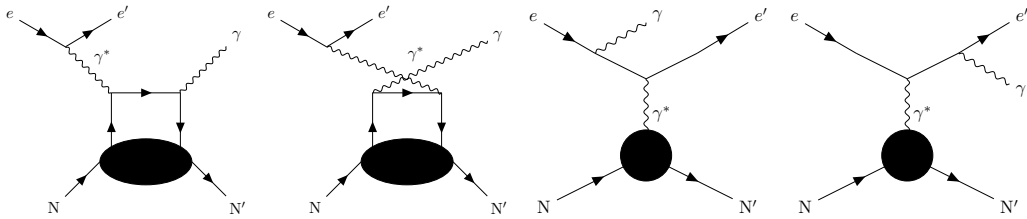


Figure 2.2: DVCS handbag diagram and BH contributions used for calculating DVCS amplitudes.

resulting expressions for the amplitudes are

$$|\mathcal{T}_{\text{BH}}|^2 = \frac{e^6(1+\varepsilon^2)^{-2}}{x_A^2 y^2 t \mathcal{P}_1(\phi) \mathcal{P}_2(\phi)} \left\{ c_0^{\text{BH}} + \sum_{n=1}^2 [c_n^{\text{BH}} \cos(n\phi) + s_n^{\text{BH}} \sin(n\phi)] \right\} \quad (2.7)$$

$$|\mathcal{T}_{\text{DVCS}}|^2 = \frac{e^6}{y^2 Q^2} \left\{ c_0^{\text{DVCS}} + \sum_{n=1}^2 [c_n^{\text{DVCS}} \cos(n\phi) + s_n^{\text{DVCS}} \sin(n\phi)] \right\} \quad (2.8)$$

$$\mathcal{I} = \frac{e^6(1+\varepsilon^2)^{-2}}{x_A y^3 t \mathcal{P}_1(\phi) \mathcal{P}_2(\phi)} \left\{ c_0^{\mathcal{I}} + \sum_{n=1}^3 [c_n^{\mathcal{I}} \cos(n\phi) + s_n^{\mathcal{I}} \sin(n\phi)] \right\} \quad (2.9)$$

The functions c_0 , c_n , and s_n are called *Fourier coefficients* and they depend on the kinematic variables and the operator decomposition of the DVCS tensor for a target with a given spin. At leading twist there is a straightforward form factor decomposition which relates the vector and axial-vector operators with the so-called Compton form factors (CFFs) [35]. The Compton form factors appearing in the DVCS amplitudes are integrals of the type

$$\mathcal{F} = \int_{-1}^1 dx F(\mp x, \xi, t) C^\pm(x, \xi) \quad (2.10)$$

where the coefficient functions at leading order take the form

$$C^\pm(x, \xi) = \frac{1}{x - \xi + i\varepsilon} \pm \frac{1}{x + \xi - i\varepsilon}. \quad (2.11)$$

We plan on measuring the beam spin asymmetry as a function of ϕ

$$A_{LU}(\phi) = \frac{d\sigma^\uparrow(\phi) - d\sigma^\downarrow(\phi)}{d\sigma^\uparrow(\phi) + d\sigma^\downarrow(\phi)} \quad (2.12)$$

where the arrows indicate the electron beam helicity.

2.1.1 DVCS Beam Spin Asymmetry

Through dominance of the Bethe-Heitler, the first sine harmonic of the beam spin asymmetry

$$A_{LU}^{\sin\phi} = \frac{1}{\pi} \int_{-\pi}^{\pi} d\phi \sin\phi A_{LU}(\phi) \quad (2.13)$$

is proportional to the following combination of Compton form factors [36]

$$A_{LU}^{\sin\phi} \propto \text{Im}(F_1 \mathcal{H} - \frac{t}{4M^2} F_2 \mathcal{E} + \frac{x_B}{2} (F_1 + F_2) \tilde{\mathcal{H}}) \quad (2.14)$$

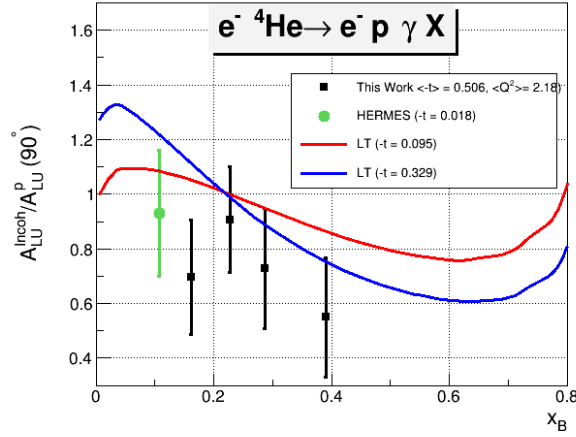


Figure 2.3: The beam spin asymmetry from eg6 [37] and HERMES along with models from Liuti and Taneja [38].

which is dominated by $\text{Im}(\mathcal{H})$ for the proton, and dominantly sensitive to $\text{Im}(\mathcal{E})$ and $\text{Im}(\tilde{\mathcal{H}})$ for the neutron.

Recent measurement [37] of incoherent DVCS by the CLAS collaboration conducted during the 6 GeV era (E08-024) have indeed shown significant modification of the proton beam spin asymmetry in ^4He without the possibility to decipher between the nuclear effects presented above. These results are shown in Fig. 2.3. In these measurements the SRC and mean field nucleons are not separated and the FSIs remain unchecked.

2.2 Tagged DVCS Reactions

The ALERT detector combined with CLAS12 provides a unique opportunity to measure incoherent exclusive processes on light nuclei. As mentioned in the previous chapters, tagging low momentum spectator recoils in exclusive knockout reactions provides the experimental leverage needed to separate and cleanly study a variety of nuclear effects.

Neutron DVCS (n-DVCS) is of immediate interest as it is needed to do a flavor separation of the GPDs. We propose to measure tagged n-DVCS on ^2H and ^4He targets starting at $P_{A-1} \simeq 70$ MeV/c for tagged protons and $P_{A-1} \simeq 120$ MeV/c for ^3He ions. The momentum densities for these targets can be seen in Fig. 2.4 and Fig. 2.5.

2.2.1 n-DVCS with a ^2H Target

Previous measurements of n-DVCS using a deuteron target required subtracting a proton contribution from the total deuteron yields [5] and assumed the validity of the PWIA. The yield for the neutron and coherent deuteron can not be separated and the subtraction yields

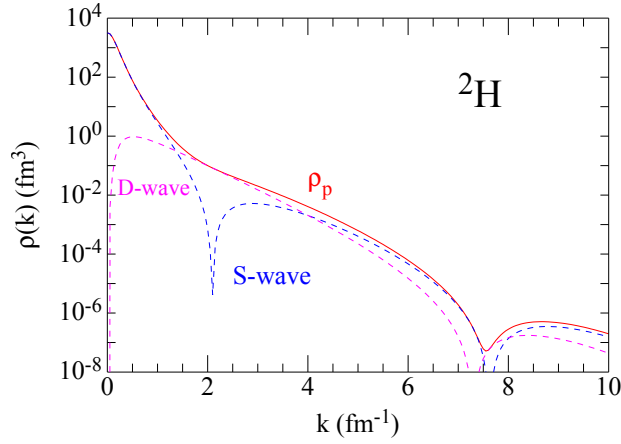


Figure 2.4: The total proton momentum distribution in the deuteron is shown by the red solid line; the contribution from S-wave and D-wave components are shown separately by blue and magenta dashed lines. [39]

the resulting beam spin asymmetry of the combination

$$D(\vec{e}, e' \gamma)X - H(\vec{e}, e' \gamma)X = d(\vec{e}, e' \gamma)d + n(\vec{e}, e' \gamma)n + \dots \quad (2.15)$$

which is fit with the CFFs of the neutron and deuteron as free parameters. This procedure has a few downsides: it requires a bin by bin equivalent proton measurement which is highly prone to systematic effects, the undetected spectator system or struck nucleon leaves the CM energy, \sqrt{s} , undetermined, and FSI remain unchecked.

We propose to measure the recoiling spectator proton, thus, measuring \sqrt{s} for every event. Furthermore, the reconstructed missing momentum can be used to check for final state interactions. Comparing t calculated from the virtual and real photon momenta to t calculated using the reconstructed missing momentum of the neutron (after selection cuts),

$$t_q = (q_1 - q_2)^2 \quad (2.16)$$

can provide a measure of the absence or presence of final state interactions.

2.2.2 n-DVCS and p-DVCS with a ^4He Target

A helium target provides the unique opportunity to again measure the neutron DVCS beam spin asymmetry, however, now on a bound nucleon with unprecedented control over final state interactions. Through the two reactions $^4\text{He}(e, e' \gamma p {}^3\text{H})$ and $^4\text{He}(e, e' \gamma {}^3\text{He})n$ the

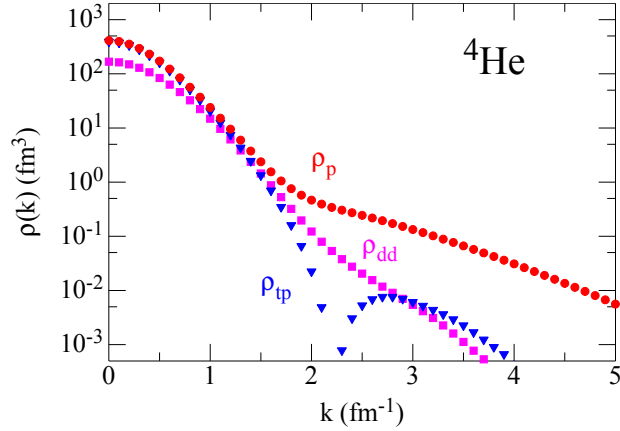


Figure 2.5: The proton momentum distribution in ${}^4\text{He}$ is shown by the red circles; the tp cluster distribution is shown by the blue triangles and the dd cluster distribution is shown by the magenta squares. [39]

ratios

$$R_n = \frac{A_{LU}^{n*}}{A_{LU}^n} \quad (2.17)$$

$$R_p = \frac{A_{LU}^{p*}}{A_{LU}^p} \quad (2.18)$$

can provide the leverage needed to definitively make a statement on medium modifications.

The proton BSA will be measured by fully detecting the final state; the struck proton will be detected in CLAS12 and the recoiling spectator ${}^3\text{H}$ will be detected in ALERT. The neutron BSA will be measured by tagging a recoil ${}^3\text{He}$, without detecting the struck neutron. Exclusivity cuts will ensure the event is cleanly selected. The free proton BSA measurement in Equation 2.17 will be taken from the already approved measurements [10, 9], while the neutron BSA will come from the measurement with a deuteron target as discussed above. The neutron measurement will have the advantage of further systematics being canceled in the ratio because the both asymmetries will come from the this experiment using identical apparatus.

Finally, we consider the fully exclusive proton DVCS reaction where a recoil triton is detected as $\mathbf{P}_{A-1} = -\mathbf{p}_1$. The fully detected final state kinematics present the opportunity to test the PWIA by requiring the two momentum transfers, t_q (Equation 2.16) and

$$t_p = (p_1 - p_2)^2 \quad (2.19)$$

to be the same, i.e., $\delta t = t_q - t_p = 0$. If a FSI occurs between the spectator and the struck nucleon (Fig. 1.4), such as pion exchange, δt will be non-zero. By selecting events where $\delta t \simeq 0$ within the detectors resolutions, we can be sure that significant final state interactions have

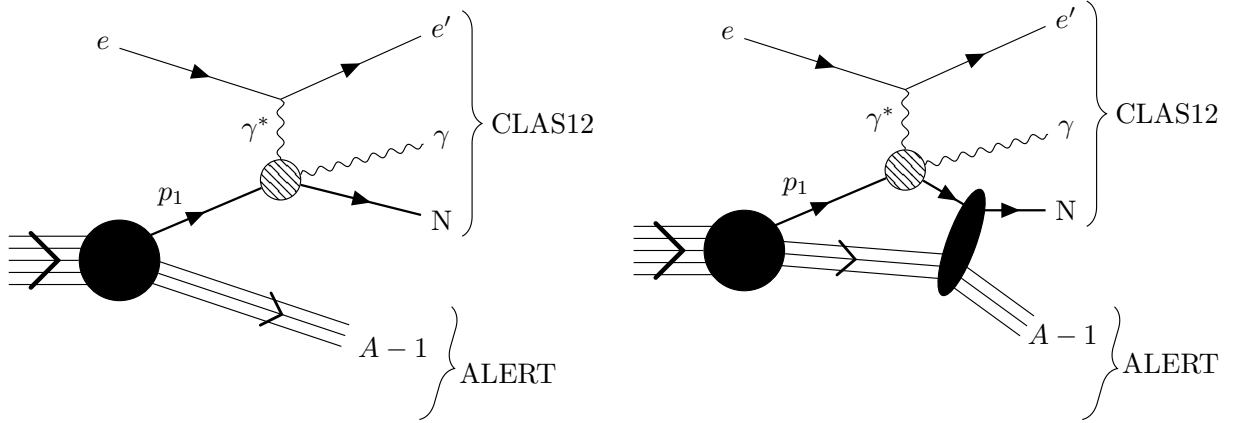


Figure 2.6: Incoherent DVCS on a nuclear target without (left) and with (right) final state interactions.

not occurred. Quite similarly, requiring the missing momentum to be back-to-back with the recoil spectator provides a cut which is expected to reduce final state interactions.

With the final state interactions well under control in the proton DVCS channel, charge symmetry suggests that the same kinematics in the neutron channel will be equally sensitive to the FSI. Therefore, the proton DVCS BSA measurement on ^4He is crucial for measuring in a model independent way the validity of the PWIA and mapping the FSIs.

Chapter 3

Experimental Setup

The different measurements of the ALERT run group require large kinematic coverage and the ability to identify the different nuclear species properly. The CLAS12 detector augmented by a low energy recoil detector is key for the success of such measurements. We summarize in Table 3.1 the requirements for the different experiments proposed in the run group.

This chapter will begin with a description of CLAS12 and the ALERT detector. After presenting the details of this new detector system, we will present an overview of the BoNuS12 RTPC followed by a discussion of how already approved or existing detectors do not satisfy the requirements for our run group.

Measurement	Particles detected	$p_{threshold}$	θ_{max}
Tagged EMC	p, ^3H , ^3He	As low as possible	As close to π as possible
Tagged DVCS	p, ^3H , ^3He	As low as possible	As close to π as possible
Nuclear GPDs	^4He	$230 < p < 400 \text{ MeV}/c$	$\pi/4 < \theta < \pi/2$ rad

Table 3.1: Requirements for the detection of low momentum spectators fragments of the proposed measurements.

3.1 The CLAS12 Forward Detector

The CLAS12 detector is designed to operate with 11 GeV beam at an electron-nucleon luminosity of $\mathcal{L} = 1 \times 10^{35} \text{ cm}^{-2}\text{s}^{-1}$. The baseline configuration of the CLAS12 detector consists of the Forward Detector and the Central Detector packages [40] (see Fig. 3.1).

The scattered electrons will be detected in the forward detector which consists of the High Threshold Cherenkov Counters (HTCC), Drift Chambers (DC), the Low Threshold

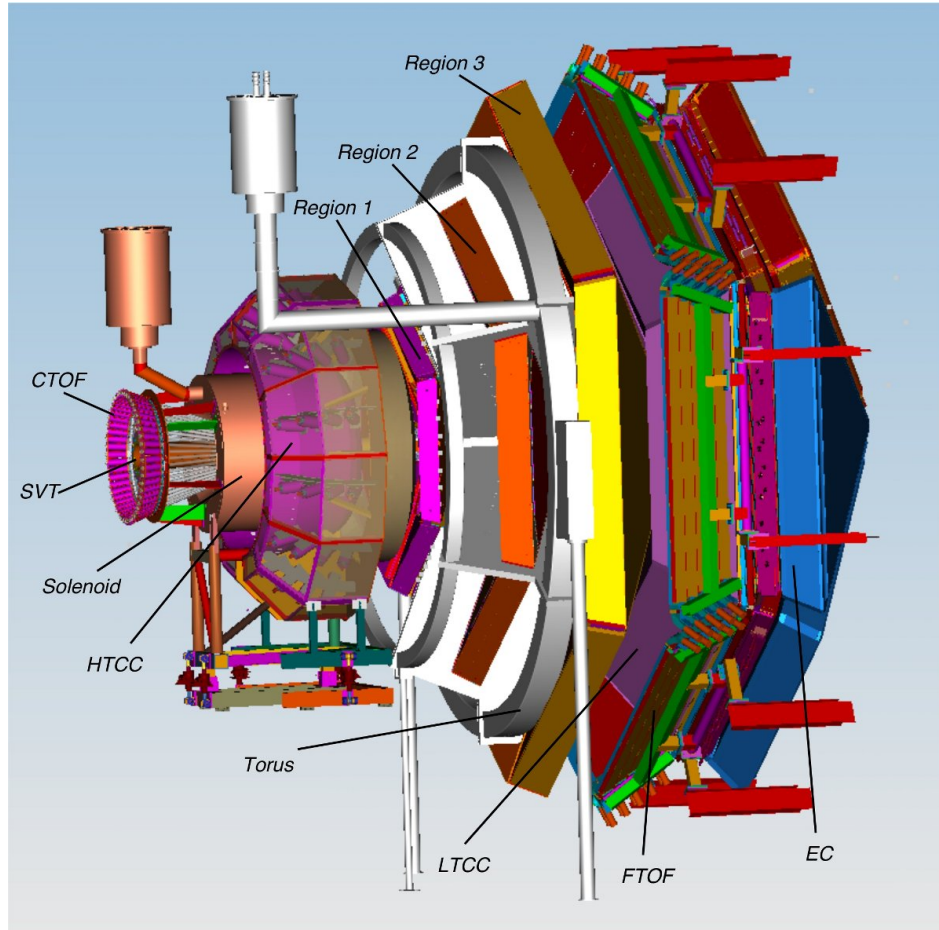


Figure 3.1: The schematic layout of the CLAS12 baseline design.

Cherenkov Counters (LTCC), the Time-of-Flight scintillators (TOF), the Forward Calorimeter and the Preshower Calorimeter. The charged particle identification in the forward detector is achieved by utilizing the combination of the HTCC, LTCC and TOF arrays with the tracking information from the Drift Chambers. The HTCC together with the Forward Calorimeter and the Preshower Calorimeter will provide a pion rejection factor of more than 2000 up to a momentum of 4.9 GeV, and a rejection factor of 100 above 4.9 GeV/c.

3.2 Design of the ALERT Detector

We propose to build a low energy recoil detector consisting of two sub-systems: a drift chamber and a scintillator hodoscope. The drift chamber will be composed of 8 layers of sense wires to provide track information while the scintillators will primarily provide particle identification. To reduce the material budget, thus pushing the energy threshold for detecting recoil particles as low as possible, the scintillator hodoscope will be placed inside the chamber, just outside of the last layer of drift wires. The good time resolution, and therefore position resolution, of the drift chamber, when coupled with the scintillators, will provide energy loss, timing, and azimuthal angle measurements for a sizable fraction of recoil particles.

The drift chamber volume will be filled with a light gas mixture (90% He and 10% C₄H₁₀) in order to not be sensitive to relativistic particles (*i.e.* electrons, gammas) and neutron backgrounds. Furthermore, a light gas mixture will increase the drift speed of electrons created during the ionization. This allows the chamber to withstand higher rates due to a shorter hit occupancy time window. The gas will likely be at atmospheric pressure but we plan to evaluate the possibility of working at a lower pressure. Based on these characteristics, the signals from this chamber and the scintillators will be used as an independent trigger, thus, reducing the DAQ trigger rate and allowing for operation at increased luminosity.

The detector must be designed to fit inside the outermost layer of Micromegas; the silicon vertex tracker and the remaining layers of Micromegas will be removed. The available space has thus an outer radius of 20 cm. A schematic layout of the preliminary design is shown in Fig. 3.2. The different detection elements are all covering about 340° of the polar angle to leave room for mechanics, and are 30 cm long with an effort made to reduce the particle energy loss through the materials. It is composed of:

- a cylindrical target, that compared to the eg6 run, is longer (~ 30 cm), wider (outer radius is 6 mm) and operating with lower pressure (~ 3 atm) in order to use a thinner target wall ($\sim 25\mu\text{m}$ Kapton)¹;

¹During the eg6 run, the pressure of the drift gas in the RTPC was ~ 1 atm, and the pressure of the target was ~ 6.5 atm. Recent tests from S. Christo (JLab) demonstrated the feasibility of a 3 atm target with a 30 μm wall, including safety margins.

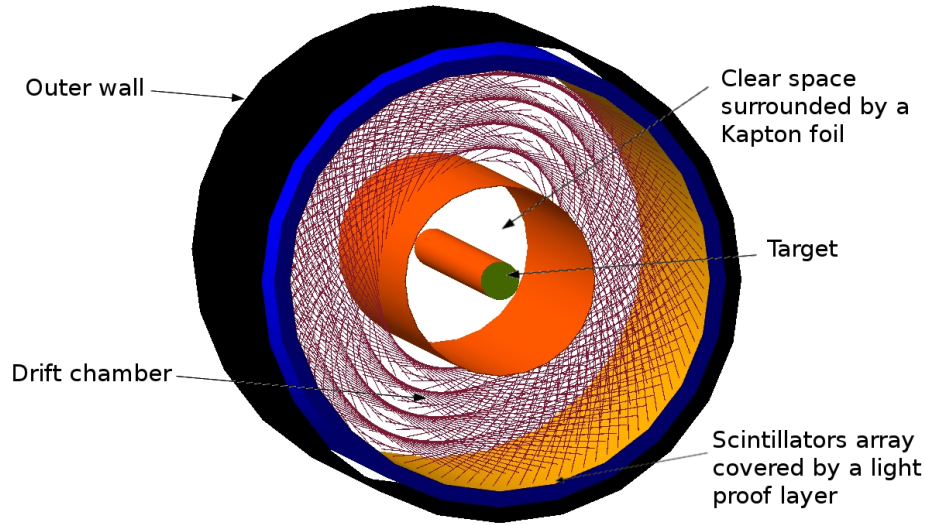


Figure 3.2: The schematic layout of the ALERT detector design, viewed from the beam direction.

- a clear space filled with helium to reduce secondary scattering from the high rate Moller electrons. Its outer radius is 30 mm;
- the drift chamber, its inner radius is 32 mm and its outer radius is 85 mm. It will detect the trajectory of the low energy nuclear recoils;
- two rings of plastic scintillators placed inside the gaseous chamber, with total thickness of roughly 20 mm.

3.2.1 The Drift Chamber

While drift chambers are very useful to cover large areas at a moderate price, huge progress has been made in terms of the ability to withstand higher rates using better electronics, shorter distance between wires and optimization of the electric field over pressure ratio. Our design is based on other chambers developed recently. For example for the dimuon arm of ALICE at CERN, drift chambers with cathode planes were built in Orsay [41]. The gap between sense wires is 2.1 mm and the distance between two cathode planes is also 2.1 mm, the wires are stretched over about 1 m. Belle II is building a cylindrical drift chamber very similar to what is needed for this experiment and for which the space between wires is around 2.5 mm [42]. Finally, a drift chamber with wire gaps of 1 mm is being built for the small wheel of ATLAS at CERN [43]. The cylindrical drift chamber proposed for our experiment is 300 mm long, and we therefore considered that a 2 mm gap between wires was technically a rather conservative goal. Optimization is

envisioned based on experience with prototypes.

The radial form of the detector does not allow for 90 degrees x-y wires in the chamber. Thus, the wires of each layer are at alternating angle of $\pm 10^\circ$, called the stereo-angle, from the axis of the drift chamber. We use stereo-angles between wires to determine the coordinate along the beam axis (z). This setting makes it possible to use a very thin forward end-plate to reduce multiple scattering of the outgoing high-energy electrons. A rough estimate of the tension due to about 2600 of 30 cm long wires is under 600 kg, which appears to be reasonable for a composite endplate.

Our drift chamber cells are composed of one sense wire made of gold plated tungsten surrounded by field wires, however the presence of the 5 T magnetic field complicates the field lines. Several cell configurations have been studied with MAGBOLTZ [44] and will be tested in a prototype (see section 3.4). For now, we decided to choose a conservative configuration as shown in Fig. 3.3. The sense wire is surrounded by 6 field wires placed equidistantly from it in a hexagonal pattern. The distance between the sense and field wires is constant and equal to 2 mm. Two adjacent cells share the field wire placed between them. The current design will have 8 layers of cells of increasing radius. The simulation code MAGBOLTZ is calculating the drift speed and drift paths of the electrons (Fig. 3.3). With a moderate electric field, the drift speed is around 10 microns/ns, the average drift time expected is thus 250 ns (over 2 mm). Assuming a conservative 10 ns time resolution, the spatial resolution is expected to be around 200 microns due to field distortions and spread of the signal.

The maximum occupancy, shown in Fig. 3.4, is expected to be of 5% for the inner most wires at $10^{35} \text{ cm}^{-2}\text{s}^{-1}$ (including the target windows). This is the maximum available luminosity for the baseline CLAS12 and is obtained based on the physics channels depicted in Fig. 3.5, assuming an integration time of 200 ns and considering a readout wire separation of 4 mm. This amount of accidental hits does not appear to be reasonable for a good tracking quality, we therefore decided to run only at half this luminosity for our main production run. This will keep occupancy below 3%, which is a reasonable amount for a drift chamber to maintain high tracking efficiency. When running the coherent processes with the ^4He target, it is not necessary to detect the protons², and the rate of accidental hits can then be highly reduced by increasing the detection threshold, thus making the chamber blind to protons³. In this configuration, considering that our main contribution to occupancy are quasi-elastic protons, we are confident that the ALERT can work properly at $10^{35} \text{ cm}^{-2}\text{s}^{-1}$.

We are currently investigating two options to read out the signals from the wires. The first option would be to use the same preamplifier as the one developed for the CLAS inner calorimeter and improved for the Heavy Photon Search [45] experiment installed in Hall B.

²This running condition is specific to the proposal “Partonic Structure of Light Nuclei” in the ALERT run group.

³The CLAS *eg6* run period was using the RTPC in the same fashion.

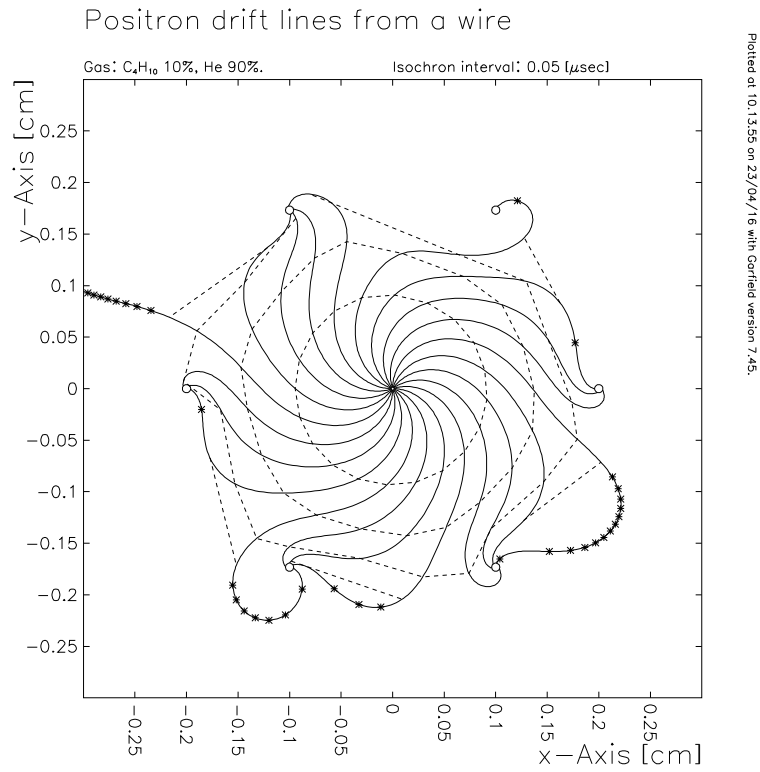


Figure 3.3: Drift lines simulated using MAGBOLTZ [44] for one sense wire (at the center) surrounded by 6 field wires. The two electric field lines leaving the cell disappear when adjusting the voltages on the wires. Dashed lines are isochrones spaced by 50 ns. This shows that the maximum drift time is about 250 ns.

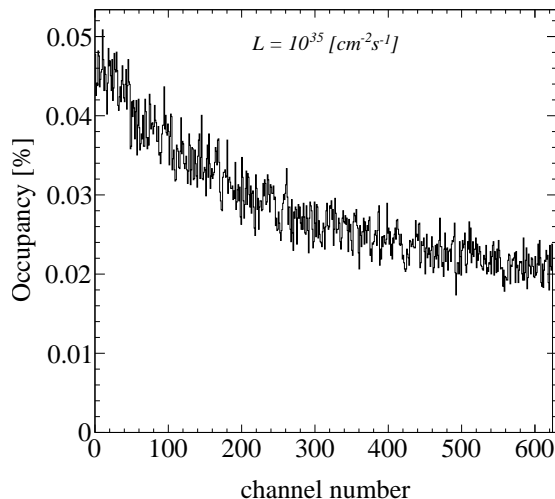


Figure 3.4: A full Geant4 simulation of the ALERT drift chamber hit occupancy at a luminosity of $10^{35} \text{ cm}^{-2}\text{s}^{-1}$. The channel numbering starts with the inner most wires and works outwards.

Depending on the gain in the drift chamber and the number of primary ionizations, it is possible to tune the gain of the preamplifier to adapt it to the needs of this experiment. More studies will be needed to evaluate how the gains of the chamber and the preamplifier can be tuned to ensure a noise that allows to select a threshold high enough to be blind to minimum ionizing particles. The time resolution of HPS has been shown to be few-hundred picoseconds for all crystals (Fig. 3.6) which is much better than our requirements.

The second option would be to use the electronics used by the Micromegas of CLAS12, known as the DREAM chip. Its dynamic range and time resolution seem to correspond to the need of our drift chamber. To ensure that it is the case, tests with a prototype will be performed (see section 3.4).

3.2.2 The scintillator array

The scintillator array will serve two main purposes. First, it will provide a useful complementary trigger signal because of its very fast response time, which will reduce the random background triggers. Second, it will provide particle identification, primarily through a time-of-flight measurement, but also by a measurement of the particle total energy deposited and path length in the scintillator which is important for doubly charged ions.

The length of the scintillators cannot exceed roughly 40 cm to keep the time resolution below 150 ps. It must also be segmented to match with tracks reconstructed in the drift chamber. Since ^3He and ^4He will travel at most a few mm in the scintillator for the highest anticipated momenta ($\sim 400 \text{ MeV}/c$), a layered scintillator design provides an extra

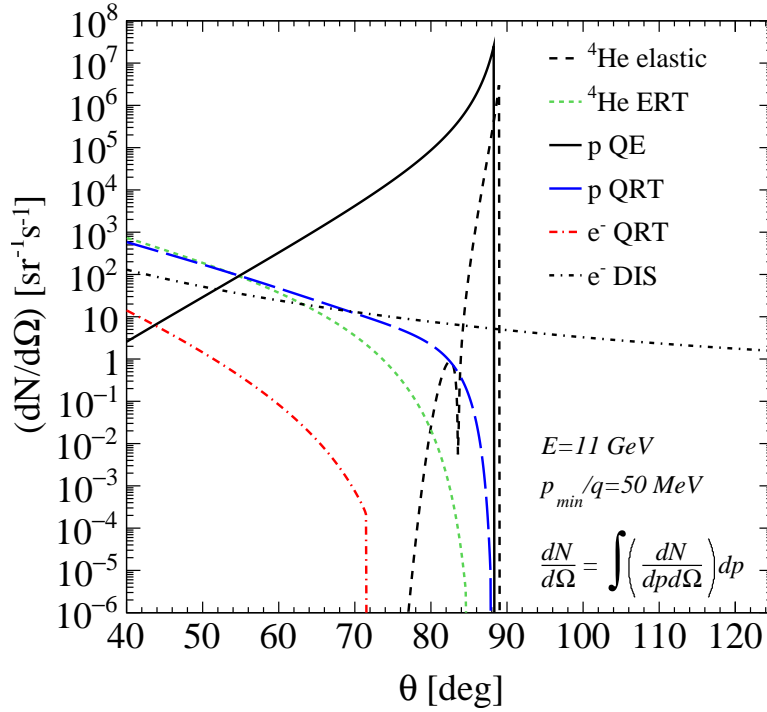


Figure 3.5: The rates for different processes as function of angle. The quasi-elastic radiative tails (QRT), ${}^4\text{He}$ elastic radiative tail (ERT), and DIS contributions have been integrated over momenta starting at $p/q = 50 \text{ MeV}/c$, where q is the electric charge of the particle detected.

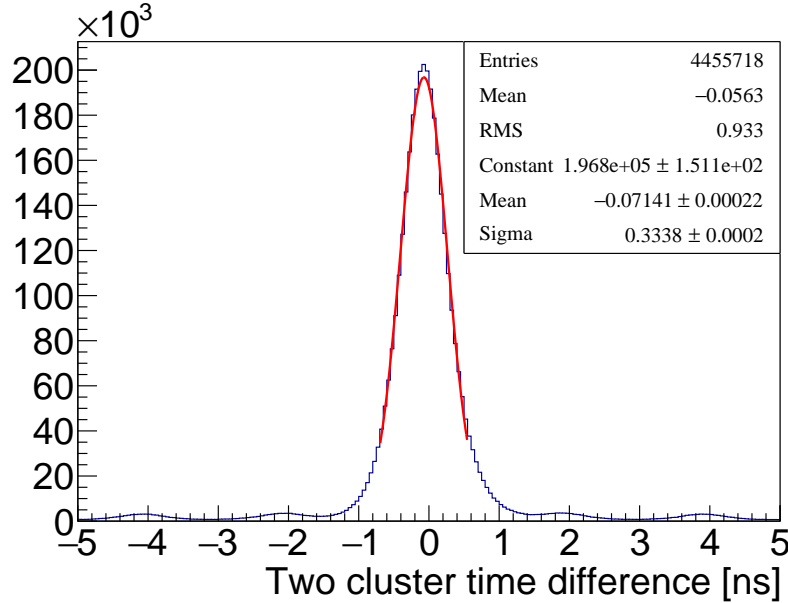


Figure 3.6: Typical time resolution of a crystal for HPS calorimeter.

handle on particle identification by checking if the range exceeded the thickness of the first scintillator layer.

The initial scintillator design consists of a thin (2 mm) inner layer of 60 bars, 30 cm in length, and 600 segmented outer scintillators (10 segments 3 cm long for each inner bar) wrapped around the drift chamber. Each of these thin inner bars has SiPM detectors attached to both ends. A thicker outer layer (18 mm) will be further segmented along the beam axis to provide position information and maintain good time resolution.

For the outer layer, a dual ended bar design and a tile design with embedded wavelength shifting fiber readouts similar to the forward tagger's hodoscope for CLAS12 [46] were considered. After simulating these designs, it was found that the time resolution was insufficient except only for the smallest of tile designs ($15 \times 15 \times 7 \text{ mm}^3$). Instead of using fibers, a SiPM will be mounted directly on the outer layer of a keystone shaped scintillator that is 30 mm in length and 18 mm thick. This design can be seen in Fig. 3.7 which shows a full Geant4 simulation of the drift chamber and scintillators. By directly mounting the SiPMs to the scintillator we collect the maximum signal in the shortest amount of time. With the large number of photons we expect, the time resolution of SiPMs will be a few tens of ps, which is well within our target.

The advantage of a dual ended readout is that the time sum is proportional to the TOF

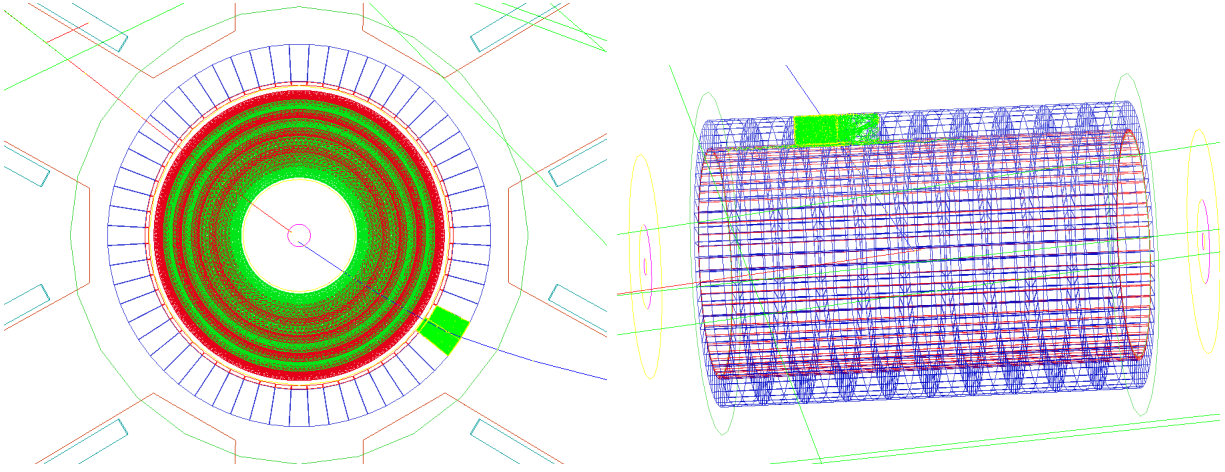


Figure 3.7: Geant4 simulation of a proton passing through the recoil drift chamber and scintillator hodoscope. The view looking downstream (left) shows the drift chamber’s eight alternating layers of wires (green and red) surrounded by the two layers of scintillator (red and blue). Simulating a proton through the detector, photons (green) are produced in a few scintillators.

plus a constant. The improved separation of different particles can be seen in Fig. 3.8. Reconstructing the position of a hit along the length of a bar in the first layer is important for the doubly charged ions because they will not penetrate deep enough to reach the second layer of segmented scintillator.

3.3 Reconstruction

The general detection and reconstruction scheme for ALERT is as follows. Fitting a track with the drift chamber and scintillator position information yields a track radius which is proportional to the transverse momentum over the charge. Next, using the scintillator time-of-flight, the particles are separated and identified by their mass-to-charge ratio, therefore leaving a degeneracy for the deuteron and α particles.

The degeneracy between deuteron and α particles can be resolved in a few ways. The first and most simple way is to observe that an α will almost never make it to the second layer and therefore the absence (presence) of a signal would indicate the particle is an α (deuteron). Furthermore, as will be discussed below, the measured dE/dx will differ for ^4He and ^2H , therefore, taking into account energy loss in track fitting alone can provide separation. Additionally taking further advantage of the measured energy deposited in the scintillators can help separate the α s and deuterons.

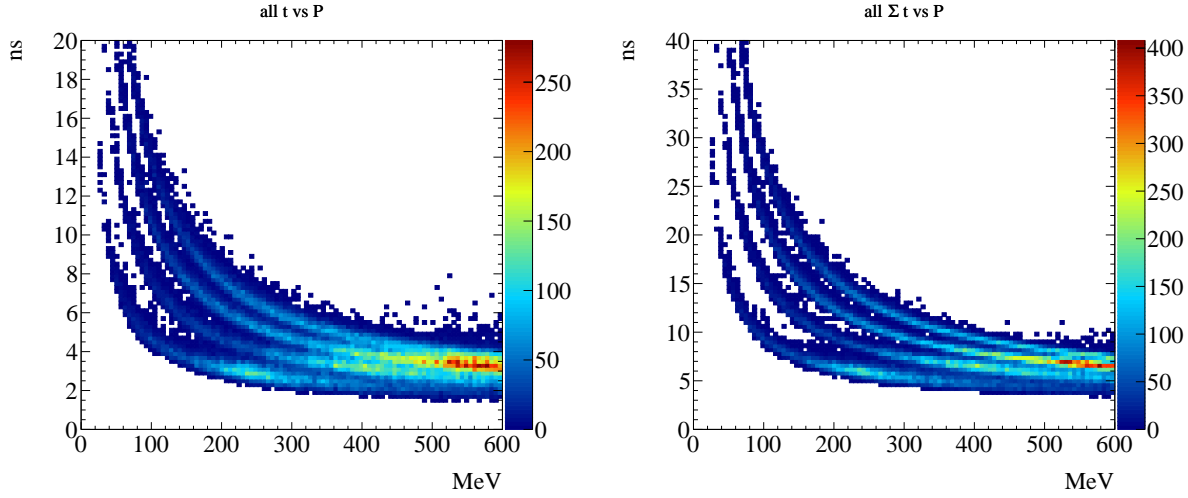


Figure 3.8: Simulated TOF for the various recoil particles vs Momentum. The TOF from just a single readout is shown on the left and the sum of the dual ended readout is shown on the right.

In the studies we present here, we do not include these latter step. However, it is important to point out that extra information is available to us in form of energy deposited in both the drift chamber and the two scintillator layers. In a full (offline) reconstruction these will give extra constraints on the identification but also on the total momentum of the detected nucleus.

As mentioned earlier, we also want a DAQ trigger, that is independent of the CLAS12 triggers. This trigger will be given by the scintillator, in coincidence with signal in a number of layers in the drift chamber. The exact number of drift chamber layers needed for the trigger will be determined during the commissioning based on actual noise and occupancy levels.

3.3.1 Track Fitting

The track obtained from a helix fitter is used to determine the coordinates of the vertex and the transverse momentum of the particle. The energy deposited in the scintillators can also be used to determine the kinetic energy of the nucleus. The feasibility and precision of the proposed vertex reconstruction and particle identification scheme were investigated with GEANT4 simulation.

The simulation of the recoil detector has been implemented with the full geometry and

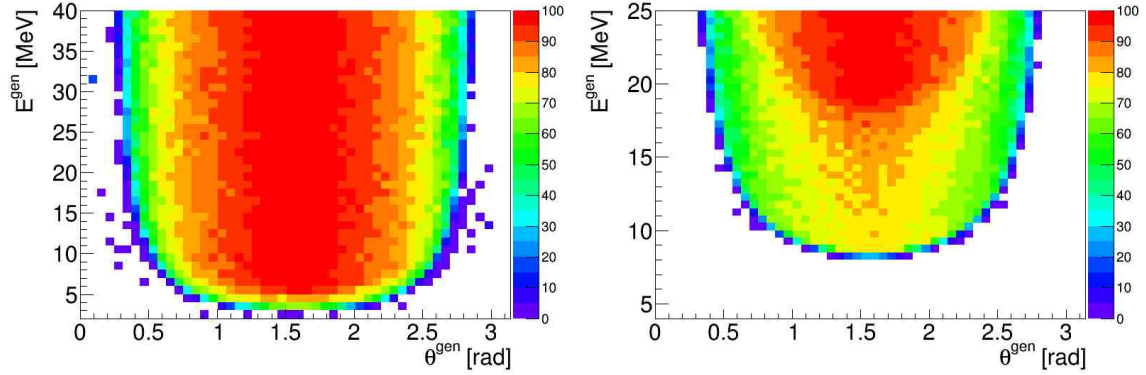


Figure 3.9: Simulated recoil detector acceptance percentage, for protons (left) and ^4He (right), when requiring energy deposition in the scintillators arrays.

material specifications. It includes a 5 Tesla homogeneous solenoid field. The entire detector is filled with a very light gas mixture of $\text{He}(90\%)$ and $\text{C}_4\text{H}_{10}(10\%)$ set at atmospheric pressure to reduce the energy loss and limit the energy deposition by minimum ionizing particles.

3.3.2 Track Reconstruction and Particle Identification

In the current study all recoil species are generated with the same distributions: flat in momentum from threshold up to 40 MeV ($\sim 250 \text{ MeV}/c$) for protons and about 25 MeV for other particles; isotropic angular coverage; flat distribution in z -vertex; and a radial vertex coordinate smeared around the beam line center by a Gaussian distribution of sigma equal to the expected beam radius (0.200 mm).

With the requirement that the particle reaches the scintillator and with a 30 cm length limit, there is a smoothly varying acceptance when averaged over the z -vertex position. This is shown from simulation in Fig. 3.9 for the lightest and heaviest recoil nuclei. However, this is a conservative estimate, since it only uses tracking information. A more elaborate PID scheme may be able to accommodate a larger acceptance for lower energy recoils.

First, the tracking capabilities of the recoil detector are investigated assuming a spatial resolutions of $200 \mu\text{m}$ for the drift chamber. The wires are strung in the z -direction with a stereo angle of 10° . For particles stopped in the scintillators, the resulting difference between generated and reconstructed variables from simulation is shown in Fig. 3.10 for ^4He particles. The momentum for protons and ^4He was also reconstructed (Fig. 3.11) from the radius of the helix assuming a uniform 5 T field. From these plots, it is clear that the resolutions required are fulfilled.

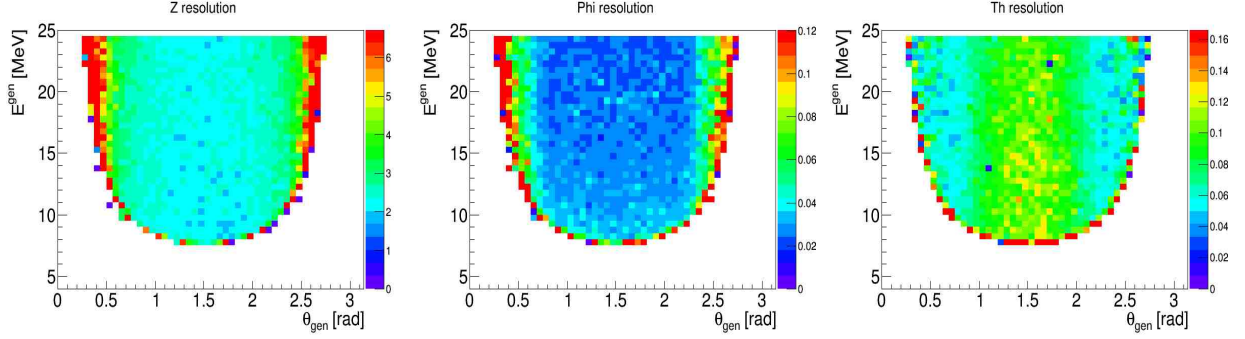


Figure 3.10: Simulated resolutions, integrated over z for ^4He , of the z -vertex (in mm) and the polar and azimuthal angles (in rad) for the lowest energy regime when the recoil track reaches the scintillator. Note the z -axis is in units of percent.

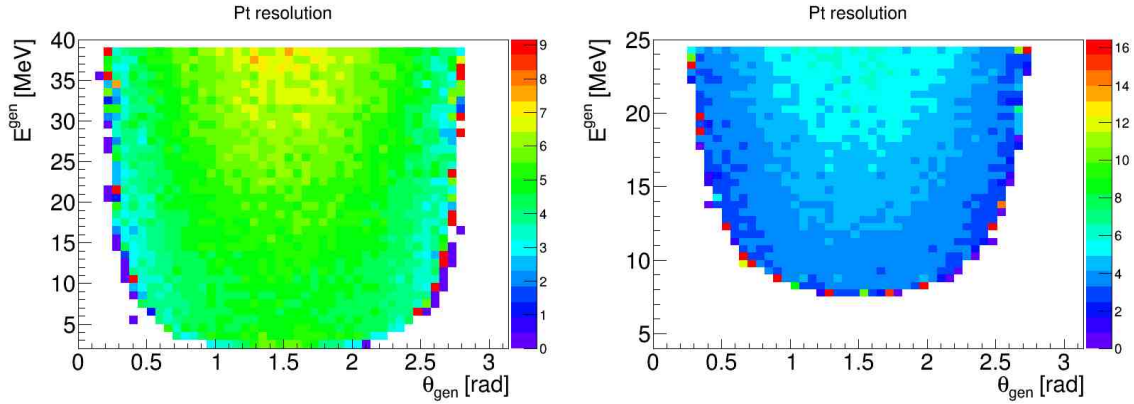


Figure 3.11: Simulated momentum resolutions for proton (left) and ^4He (right) integrated over z , when the recoil track reaches the scintillators array. Note the z -axis is in units of percent.

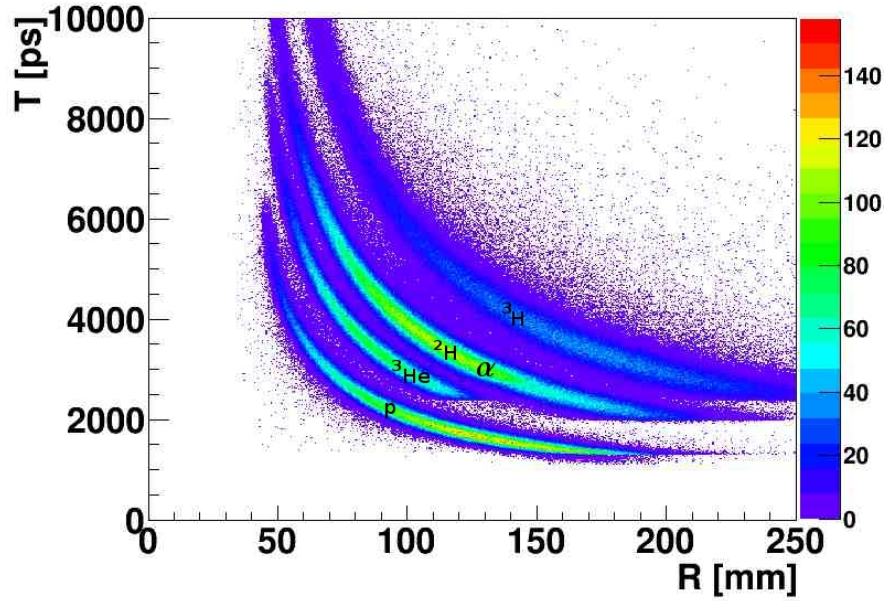


Figure 3.12: Simulated time of flight at the scintillator versus the reconstructed radius in the drift chamber. The bottom band corresponds to proton, next band is the ^3He nuclei, ^2H and α are overlapping in the third band, the uppermost band is ^3H . ^2H and α are separated using dE/dx .

Next, the particle identification scheme is investigated. The scintillators have been designed to ensure a 150 ps time resolution. To determine the dE/dx resolution, measurements will be necessary for the scintillators and for the drift chamber as this depends on the detector layout, gas mixture, its electronics, voltages... Nevertheless, from [47], one can assume that with the 8 drift chamber measurements and the measurements in the scintillators, the energy resolution should be around 10% or better.

Under those conditions, a clean separation of three of the five nuclei is shown in Fig. 3.12 which represents the time of arrival in the scintillator as a function of the reconstructed radius in the drift chamber. ^2H and α are separated using dE/dx in the drift chamber and in the scintillators.

To quantify the separation power of our device, we simulated an equal quantity of each species. We obtained a particle identification efficiency of 99% for protons, 95% for ^3He and 98% for ^3H and around 90% for ^2H and α with equally excellent rejection factors. It is important to note that for this analysis, only the energy deposited in the scintillators was used, not the energy deposited in the drift chamber nor the path length in the scintillators, thus

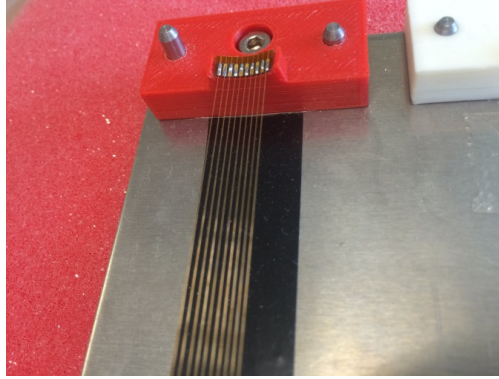


Figure 3.13: Welded wires on a curved structure with a 2 mm gap between each wire.

these number are very conservative. This analysis suggests that the proposed reconstruction and particle identification schemes for this design are quite promising. Studies, using both software and prototyping, are ongoing to determine the optimal detector parameters to minimize the detection threshold while maximizing particle identification efficiency. The resolutions presented above have been implemented in a fast Monte-Carlo used in the next section to evaluate the impact on our measurements.

3.4 Drift chamber prototype

Since the design of the drift chamber presents several challenges, we decided early to start the R&D for the project and build a prototype to investigate the feasibility. This section presents the work done in Orsay to address the main questions concerning the mechanics that needed to be answered:

- Can we build a stereo drift chamber with a 2 mm gap between wires?
- Can we design a frame that can be quickly changed in case of a broken wire?
- Can the forward structure be both light to reduce the multiple scattering and rigid enough to support the tension due to the wires?

For the first question, small plastic structures realized with a 3D printer were tested and wires welded on it, as shown in Fig. 3.13. This demonstrated our ability to weld wires with a 2 mm gap on a curved structure.

To limit issues related to broken wires, we opted for a modular detector made of identical sectors. Each sector covers 20° of the azimuthal angle (Fig. 3.14) and can be rotated around the beam axis to be separated from the other sectors. This rotation is possible due to the absence of one sector, leaving a 20° dead angle. Then, if a wire breaks, its sector can be

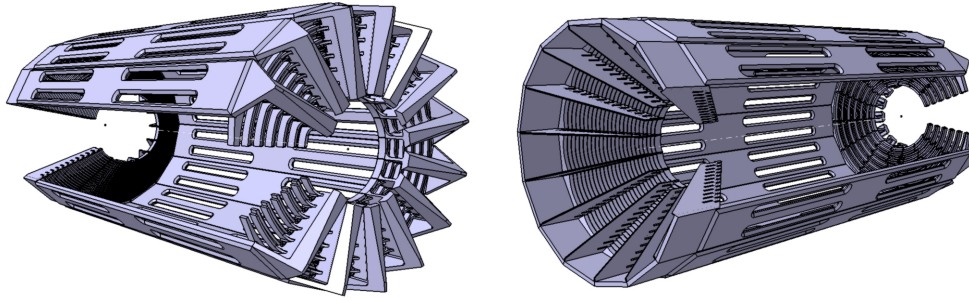


Figure 3.14: Upstream (left) and downstream (right) ends of the prototype detector in CAD with all the sectors included.

removed independently and replaced by a spare. Plastic and metallic prototype sectors were made with 3D printers to test the assembling procedure and we have started the construction of a full size prototype of one sector.

The shape of each sector is constrained by the position of the wires. It has a triangular shape on one side and due to the stereo angle, the other side looks like a pine tree with branches alternatively going left and right from a central trunk (Fig. 3.15).

The last question about the material used to build the structure will be studied in details with future prototypes. Nevertheless, current design plans are to use carbon in place of the aluminum in the forward region and titanium for the backward structure. The prototype was designed to check the mechanical requirements summarized above but also to verify the different cell configurations, and to test the DREAM electronics (time resolution, active range, noise). Since a total of five sectors have been build for tests, this will allow us to check that the elements can be properly positioned relatively to each other and one sector will be completely equipped with wires to be tested with a cosmic test bench and an α source.

3.5 Other options for a Low Energy Recoil Detector

We explored other available solutions for the low-energy recoil tracker (ALERT) with adequate momentum and spatial resolution, and good particle identification for recoiling light nuclei (p , ^3H and ^3He). After investigating the feasibility of the proposed measurements using the CLAS12 Central Detector and the BoNuS Detector [18, 19], we concluded that we needed to build a dedicated detector. We summarize in the following the facts that led us to this conclusion.

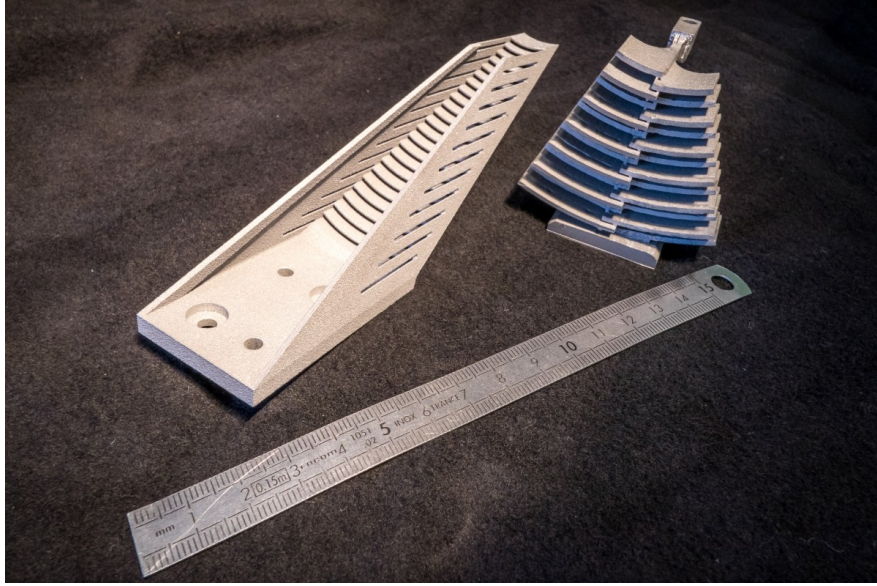


Figure 3.15: Mechanics of one sector for the prototype made with 3D printer.

3.5.1 Central Detector

The CLAS12 Central Detector [40] is designed to detect various charged particles over a wide momentum and angular range. The main detector package includes:

- Solenoid Magnet: provides a central longitudinal magnetic field up to 5 Tesla, serves to curl emitted low energy Møller electrons and determine particle momenta through tracking.
- Central Tracker: consists of 3 layers of silicon strips and 3 layers of Micromegas. The thickness of a single silicon layer is $300\mu\text{m}$.
- Central Time-of-Flight: an array of scintillator paddles with a cylindrical geometry of radius 26 cm and length 50 cm; the thickness of the detector is 2 cm with designed timing resolution of $\sigma_t = 50$ ps, used to separate pions and protons up to $1.2 \text{ GeV}/c$.

The current design, however, is not optimal for low energy particles ($p < 300 \text{ MeV}/c$) due to the energy loss in the first 2 silicon strip layers. The momentum detection threshold is $\sim 200 \text{ MeV}/c$ for protons, $\sim 350 \text{ MeV}/c$ for deuterons and even higher for ^3H and ^3He . These values are significantly too large for our proposed measurements, which makes the CLAS12 central detector not suitable for our measurements.

Detectors	RTPC	New Tracker
Drift region radius	4 cm	5 cm
Longitudinal length	~ 40 cm	~ 40 cm
Gas mixture	80% helium/20% DME	90% helium/10% isobutane
Azimuthal coverage	360°	340°
Momentum range	70-250 MeV/ c protons	70-250 MeV/ c protons
Transverse mom. resolution	10% for 100 MeV/ c protons	10% for 100 MeV/ c protons
z resolution	3 mm	3 mm
Solenoidal field	~ 5 T	~ 5 T
ID all light nuclei	No	Yes
Trigger	can not be included	can be included

Table 3.2: Comparison between the RTPC (left column) and the new tracker (right column).

3.5.2 BoNuS12 Radial Time Projection Chamber

The original BoNuS detector was built for Hall B experiment E03-012 to study neutron structure at high x_B by scattering electrons off an almost on-shell neutron inside deuteron. The purpose of the detector was to tag the low energy recoil protons ($p > 60$ MeV/ c). The key component for detecting the slow protons was the Radial Time Projection Chamber (RTPC) based on Gas Electron Multipliers (GEM). A later run period (eg6) used a ^4He gas target and a newly built and improved RTPC to detect recoiling α particles in coherent DVCS scattering. The major improvements of the eg6 RTPC were full cylindrical coverage and a higher data taking rate.

The approved 12 GeV BoNuS (BoNuS12) proposal is planning to use a similar device with some upgrades. The target gas cell length will be doubled, and the new RTPC will be longer as well, leading to a doubling in luminosity and an increased acceptance. Taking advantage of the larger bore (~ 700 mm) of the 5 Tesla solenoid magnet, the maximum radial drift length will be increased from the present 3 cm to 4 cm, improving the momentum resolution by 50% [19] and extending the momentum coverage. The main features of the proposed BoNuS12 detector are summarized in Table 3.2.

In principle, particle identification can be obtained from the RTPC through the energy loss dE/dx in the detector as a function of the particle momentum (see Fig. 3.16). However, with such a small difference between ^3H and ^3He , it is nearly impossible to discriminate between them on an event by event basis because of the intrinsic width of the dE/dx distributions. This feature is not problematic when using deuterium target, but makes the RTPC no longer a viable option for our tagged EMC and tagged DVCS measurements which require a ^4He target and the detection of ^4He , ^3He , ^3H , deuterons and protons.

Another issue with the RTPC is its slow response time due to the long drift time

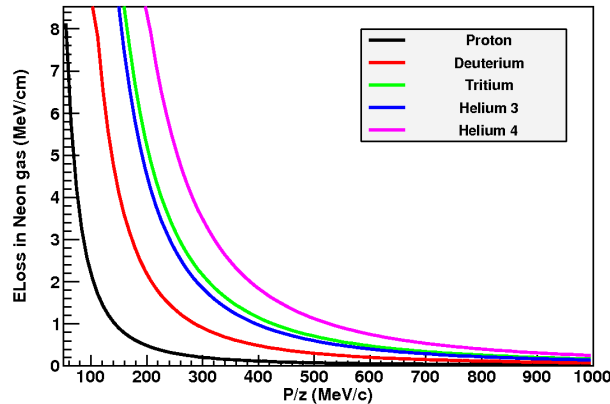


Figure 3.16: Calculation of energy loss in Neon gas as a function of the particle momentum divided by its charge for different nuclei.

($\sim 5\mu\text{s}$). If a fast recoil detector could be included in the trigger it would have a significant impact on the background rejection. Indeed, in about 90% DIS on deuteron or helium the spectator fragments have too low energy or too small angle with the beam line to get out of the target to be detected. Since the data acquisition speed was the main limiting factor for both BoNuS and eg6 runs in CLAS, including the recoil detector in the trigger would allow us to run at higher luminosities. Indeed events without a hit in the recoil detector would not be recorded and this will significantly reduce the trigger's frequency.

3.5.3 Summary

As explained in the previous sections, the threshold of the CLAS12 inner tracker is clearly too high to be used for our measurements. On the other hand, the recoil detector planned for BoNuS12, a RTPC, is not suitable due to its inability to distinguish all kind of particles we need to measure. Moreover, as the RTPC cannot be efficiently included in the trigger, a lot of background events are sent to the readout electronics, which will cause its saturation and limit the maximum luminosity the detector can handle. Therefore, we propose to use A Low Energy Recoil Tracker (ALERT) based on a new detector design, described in the previous sections, that would provide good timing and energy loss information and a total energy measurement for each track. The fast timing will allow a tight time coincidence with CLAS12, thereby reducing the background that was encountered in previous RTPC detectors. The recoil detector can be included in the data acquisition trigger, which will significantly reduce triggering on events from the target windows, which are outside the acceptance and events with recoil too slow to exit the target.

Finally, the use of time of flight and dE/dx measurements will provide improved particle

identification for the recoiling nuclei without ambiguity for ^3H and ^3He identification. The features and requirements for this new detector are compared with the current RTPC design for BoNuS12 in Table 3.2. The transverse momentum and z resolution are chosen following the BoNuS specifications.

3.6 Technical contributions from the research groups

This effort is led by four research groups, Argonne National Lab (ANL), Institut de Physique Nucléaire d'Orsay (IPNO), Jefferson Lab and Temple University (TU).

Jefferson Lab is the host institution. ANL, IPNO and TU have all contributed technically to CLAS12. ANL was involved in the construction of the high-threshold Cherenkov counters (HTCC) for CLAS12. ANL has a memorandum of understanding (MOU) with JLab on taking responsibility for the HTCC light collection system including testing the photomultipliers and the magnetic shielding. For the RICH detector for CLAS12, ANL developed full GEANT-4 simulations in addition to the tracking software. ANL also developed the mechanical design of the detector support elements and entrance and exit windows in addition to the front-end electronics cooling system. IPNO took full responsibility for the design and construction of CLAS12 neutron detector (CND). The CND was successfully delivered to Jefferson Lab. TU played an important role in the refurbishment of the low threshold Cherenkov counters (LTCC), which was completed recently. All 216 photomultipliers have been coated with wavelength shifting material (p-Terphenyl) at Temple University, which resulted in a significant increase in the number of photoelectrons response.

The three institutions have already shown strong technical commitment to JLab 12 GeV upgrade, with a focus on CLAS12 and this proposal is a continuation of that commitment.

3.6.1 Argonne National Laboratory and Temple University

The ANL medium energy group is responsible for the ALERT scintillator system, including scintillation material, light collection device and electronics. First results of simulations have led to the design proposed here. This work will continue to integrate the scintillator system with the wire chamber. ANL will collaborate closely with Temple University to test the light detection system. Both institutions will be responsible to assemble and test the detector.

3.6.2 Institut de Physique Nucléaire d'Orsay

The Institut de Physique Nucléaire d'Orsay is responsible for the wire chamber and the mechanical structure of the detector design and construction. As shown in the proposal, this work has already started as part of a wider R&D program focused on nuclear fragments

detection with light wire chambers. A first prototype is being built to test different cell forms, wire material, wire thickness, pressure, etc. This experience will lead to a complete design of the ALERT detector integrating the scintillator built at ANL, the gas distribution system and the electronic connections. The funding already secured for this program should allow for the construction of these mechanical parts and the wire chamber itself.

Funding is also available, in partnership with *CEA Saclay*, to test the use of the DREAM front-end chip for our wire chamber. Further tests are planned to adapt the electronics to the ALERT chamber or test other chips. This chip will be used for the CLAS Micromegas, so we expect its integration to be straightforward when the ALERT run group will need it.

3.6.3 Jefferson Laboratory

We expect Jefferson Laboratory to help with the settings of the beam line. In particular, the maximum beam current will be around 500 nA for the run at $10^{35} \text{ cm}^{-2}\text{s}^{-1}$, which is not common for Hall-B. We also expect JLab to design and build the target for the experiment as it will be a very similar target as the ones build for CLAS Bonus and eg6 run.

We also expect Jefferson Laboratory to provide assistance in the detector installation in the Hall and to connect the electronics of ALERT to the acquisition and trigger systems of CLAS12 in addition to slow controls.

Chapter 4

Proposed Measurements

We propose to measure the beam spin asymmetry for three DVCS channels using two different targets and with tagged spectator systems. The three principal reactions are:

- ${}^4\text{He}(\vec{e}, e' \gamma {}^3\text{H}p)$ – bound p-DVCS
- ${}^4\text{H}(\vec{e}, e' \gamma {}^3\text{He})n$ – bound n-DVCS
- ${}^2\text{H}(\vec{e}, e' \gamma p)n$ – quasi-free n-DVCS

where in the first process the final state is fully detected. Before discussing the details of the measurements, we present an overview of the procedure for extracting the $\sin \phi$ harmonic of the BSAs and identify the primary deliverables of the experiment.

4.1 Asymmetry Extraction Procedure

Fig. 4.1 shows how, starting with just one kinematic bin in t , Q^2 , and x (which is not explicitly shown), the BSA is extracted for three regions of spectator recoil angles relative to the virtual photon direction and three ranges of spectator momenta. As indicated, the spectator angles correspond to a forward tagged system, a system with perpendicular momenta, and a backward tagged spectator. In the latter angular region, FSIs are expected to be minimal. Furthermore, three ranges of momenta are identified, the lowest corresponding to nucleons moving in the mean field and the highest belonging to nucleons in short range correlated pairs. Fitting the BSA asymmetries yields the $\sin \phi$ harmonic which is shown on the right Fig. 4.1 for the different spectator kinematic regions.

The first process above, p-DVCS on ${}^4\text{He}$, provides a model independent way of identifying kinematics where final state interactions are minimized (see Introduction and Chapter 1). Armed with this information we will then measure the n-DVCS beam spin asymmetries on ${}^4\text{He}$ and ${}^2\text{H}$ knowing which kinematics are, or are not, influenced by FSIs. We will then proceed as shown in Fig. 4.2 where the two n-DVCS measurements are combined into a

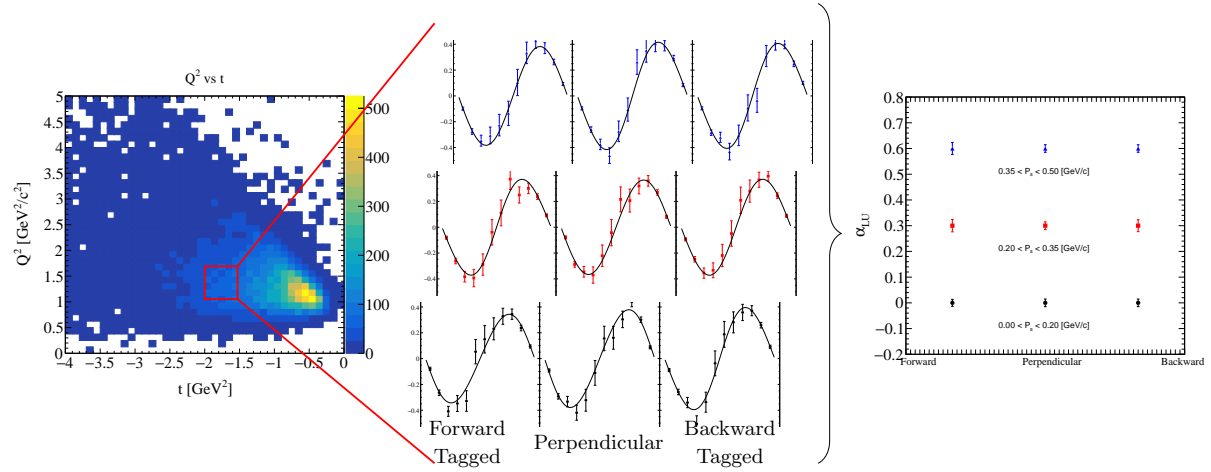


Figure 4.1: A general overview of the BSA extraction procedure for a kinematic bin. For each (x, Q^2, t) bin the BSA is extracted through fitting the asymmetry as function of ϕ (see Equation 4.1) for the various spectator momentum configurations and the $\sin \phi$ harmonic, α is extracted. Note these plots are only showing statistical uncertainties and the values are offset for clarity.

ratio of bound neutron to quasi-free neutron. These BSA measurements and ratios are the primary deliverables of this proposal. They will be measured over a broad range of DVCS kinematics accessible to CLAS12 and for the spectator momenta regions noted above using the ALERT detector.

4.2 Kinematic Coverage

The kinematic coverage was studied using a newly developed CLAS12 fast Monte-Carlo, `c12sim`, where the CLAS12 detector resolutions were replicated based on the Fortran CLAS12 Fast-MC code. Because `c12sim` is a Geant4 based simulation, the particle transport through the magnetic fields was handled by the Geant4 geometry navigation where all other processes were turned off. The resolutions for ALERT were obtained through full Geant4 simulations with all physics processes turned on.

First consider the p-DVCS reaction on ${}^4\text{He}$ because of its special ability to determine the presence of final state interactions through a fully detected final state. The spectator system, a recoiling ${}^3\text{H}$ in the present case, is detected in ALERT while the forward electron, photon, and proton are detected in CLAS12. The resulting kinematics for the n-DVCS on ${}^2\text{H}$ and ${}^4\text{He}$ reactions will be quite similar, where the key difference is the struck neutron goes undetected. These events are then selected via the neutron missing mass.

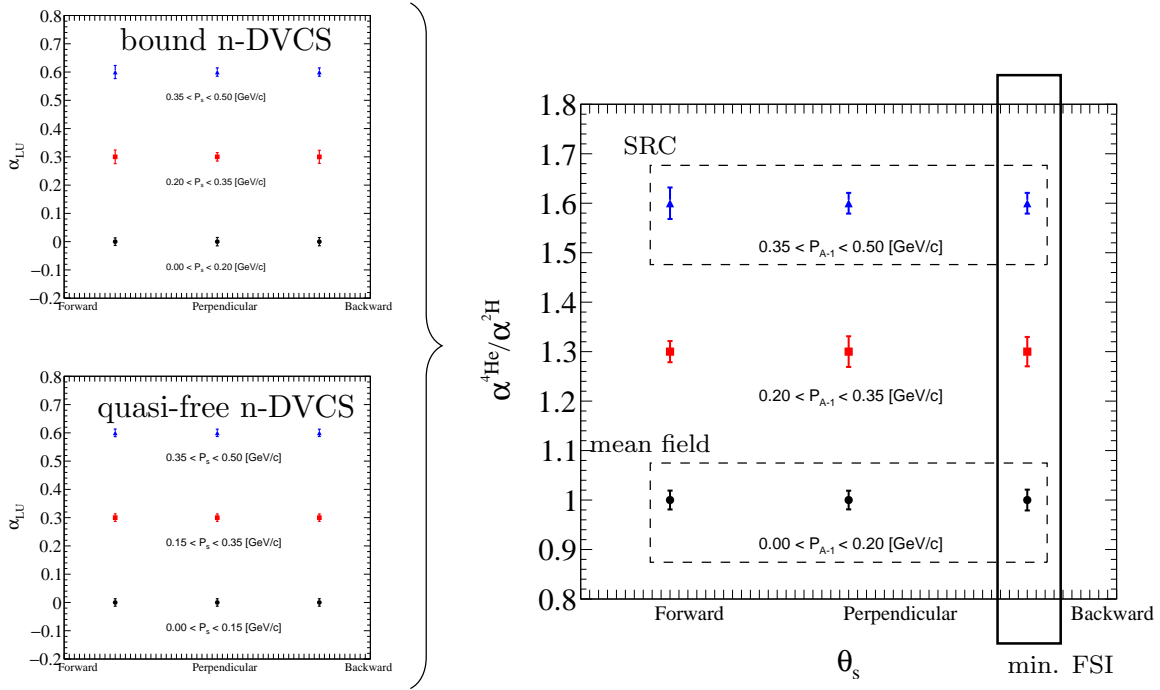


Figure 4.2: The BSA ratios targeting different nuclear effects with specific spectator kinematics. Note only statistical uncertainties are shown and the BSA harmonics/ratios are (arbitrarily) offset for clarity.

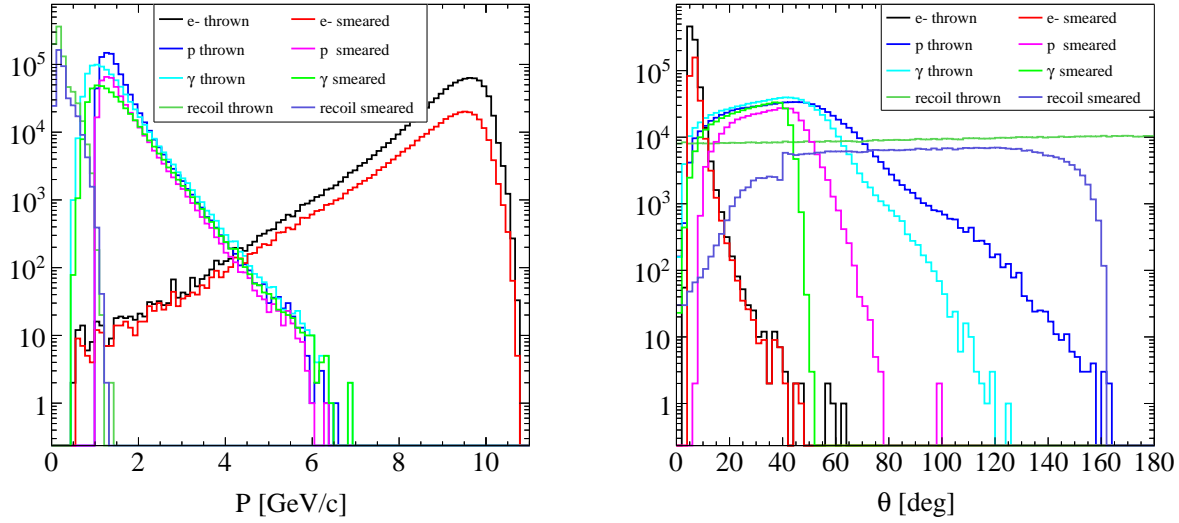


Figure 4.3: The thrown and detected momentum (left) and angular (right) distributions showing overall acceptance for the experiment.

The overall coverage in momentum and scattering angle can be seen in Fig. 4.3 and angular acceptance of all the particles can be seen Fig. B.6. The bin variables x , Q^2 , and t are shown in Fig. 4.6, and the spectator variables, θ_s and P_{A-1} , are shown in Fig. 4.7.

As mentioned in Chapter 1, the momentum transfer can be reconstructed via Equation 2.16 using the photons, or through Equation 2.19 where we make use of the measured spectator recoil momentum and the reconstructed momentum of the struck proton. Fig. B.1 shows that the resolutions are comparable, thus, allowing for the systematic check of FSIs. The spectator angle and momentum can be seen in Fig. 4.7, where these results can be used along with calculations such as those shown in Fig. 1.6 to isolate FSIs.

4.3 Projections

4.3.1 Beam Spin Asymmetry Extraction

The measured beam spin asymmetries are binned in 6 variables: x_B , Q^2 , t , ϕ , P_s , and θ_s . The 6 dimensional data will be reduced to 5 dimensions by fitting the BSA as a function of ϕ . Projections for the statistical uncertainties of these asymmetries and their fits are shown for a few bins in Fig. 4.8 and Fig. 4.9 for p-DVCS on ^4He . A few of the ϕ binned asymmetries for n-DVCS on ^4He are shown in Fig. 4.10 and similarly in Fig. 4.11 for n-DVCS on ^2H . Note that we are using a simple binning scheme shown in Table 4.1. These bins are likely to change as the cross sections are not well known, especially when isolating high momentum spectators.

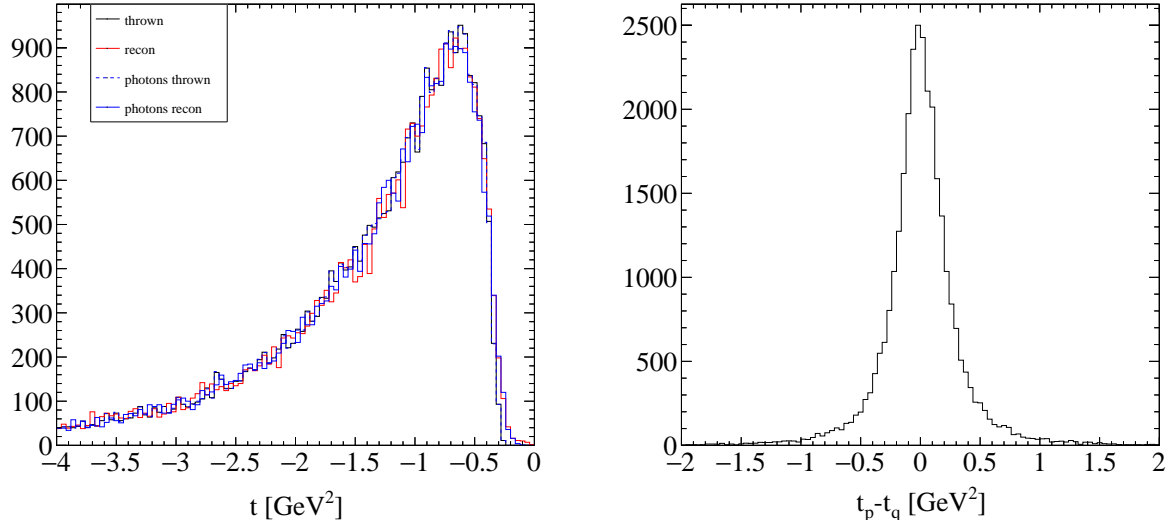


Figure 4.4: Left: Thrown and reconstructed t calculated from the photons (t_q) and hadrons (t_p). Right: The difference between the two momentum transfers, $\delta t = t_p - t_q$.

Bin					
x	0.05	0.25	0.35	0.5	0.8
Q^2 [GeV ²]	1	1.5	2.0	3.0	10
t [GeV ²]	0	0.75	1.5	2.5	6.0
θ_s [degrees]	0.0	50	100	180	
P_s [GeV/c]	0.0	0.2	0.45	1.0	

Table 4.1: The simple binning scheme used for the proposal. Listed here are the bin edges forming each.

The beam spin asymmetries are the primary observables for this experiment and will be fit with the following simplified parameterization

$$A_{LU}(\phi) = \frac{\alpha \sin \phi}{1 + \beta \cos \phi} \quad (4.1)$$

where the free parameters α and β are related to CFFs and Fourier harmonics. As emphasized in section 1.2.2, the $\sin \phi$ harmonic, α , is quite sensitive to nuclear effects. Therefore, we will extract α for every bin by fitting the asymmetry binned in ϕ for each kinematic setting. Out of the many kinematic settings, Fig. 4.12 (left) shows the result of fitting the ϕ asymmetry for one bin in x , Q^2 , and t .

For the n-DVCS measurements, the missing mass cut will select DVCS events. The primary assumption is what we will have already observed through the p-DVCS channel and isolated kinematics where FSIs are minimized. This is typically backwards low momentum

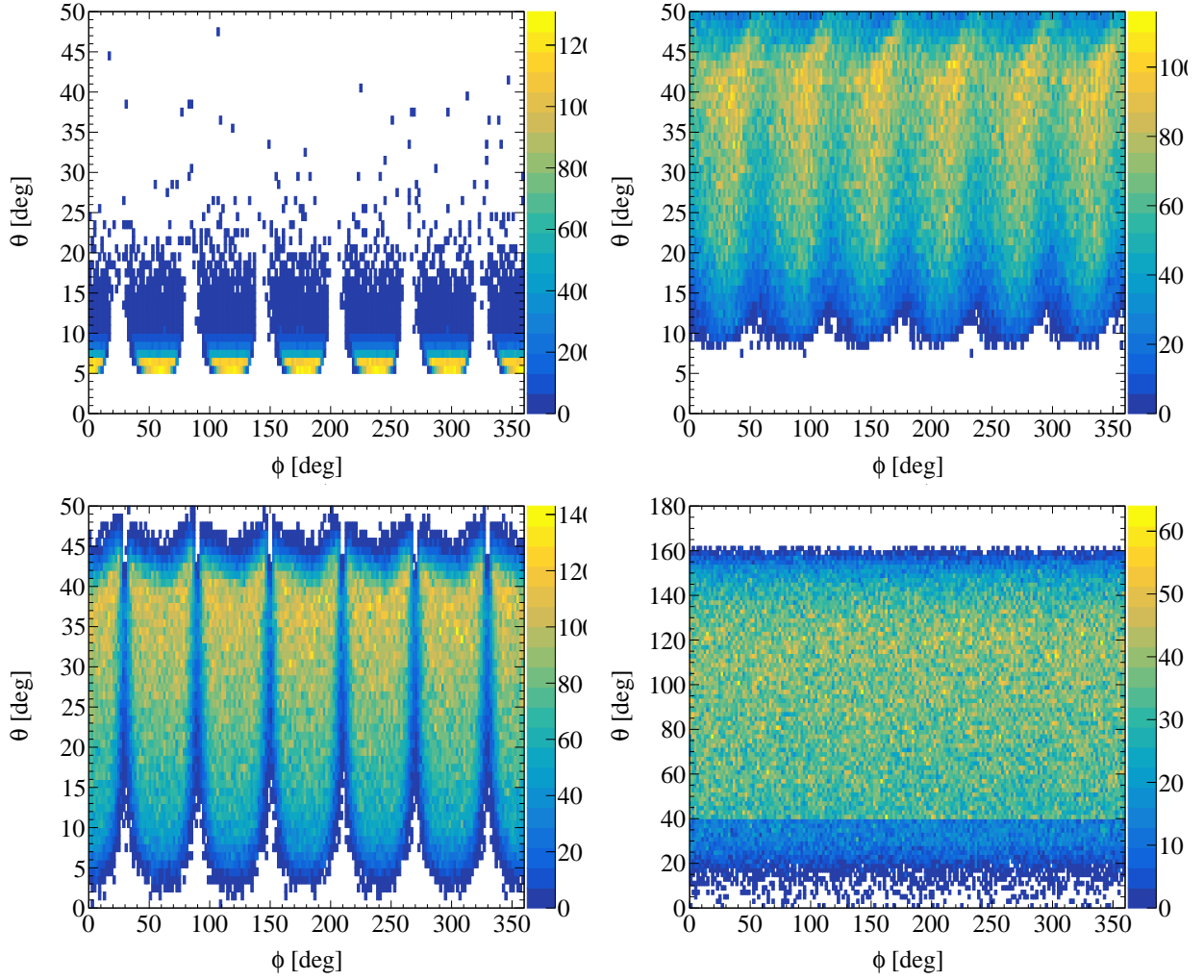


Figure 4.5: The directional acceptance shown as θ Vs. ϕ for the electron (upper left), proton (upper right), photon (lower left), and recoil spectator (lower right).

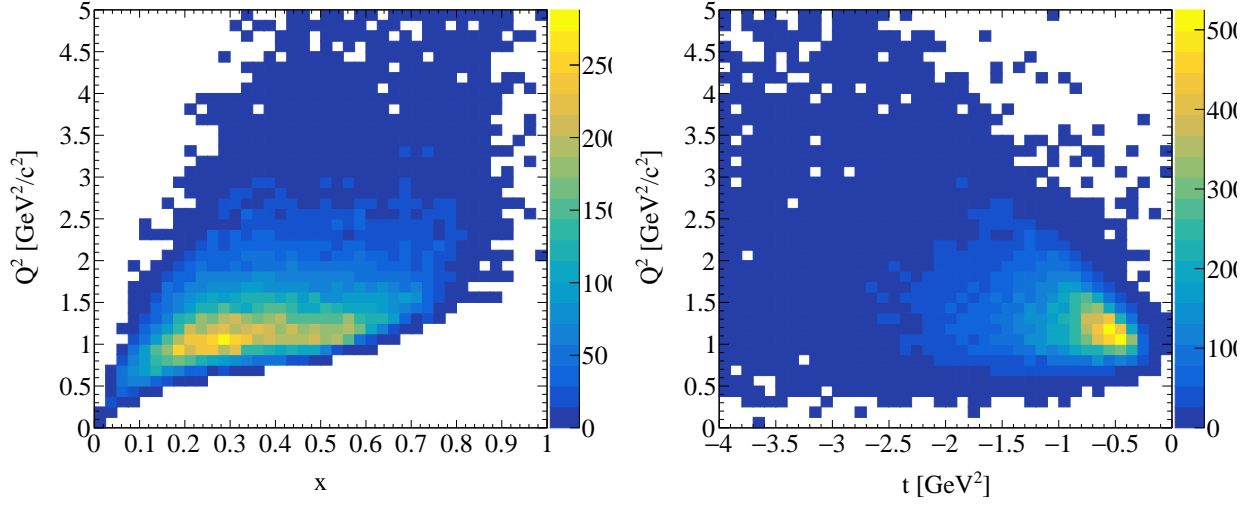


Figure 4.6: Q^2 plotted against x (left) and t (right).

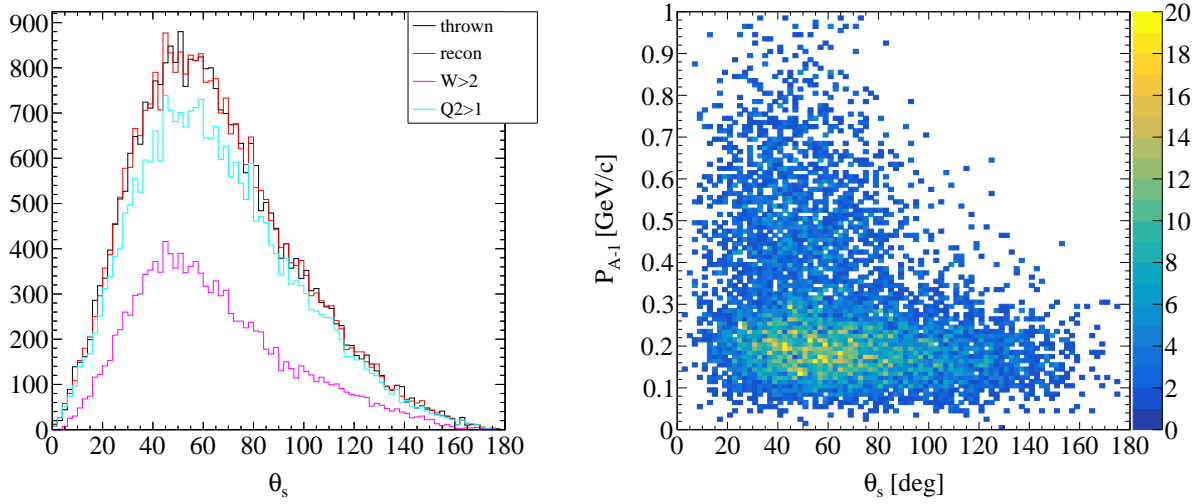


Figure 4.7: Left: Coverage of the spectator recoil angle, θ_s . Right: Spectator angle vs reconstructed spectator momentum.

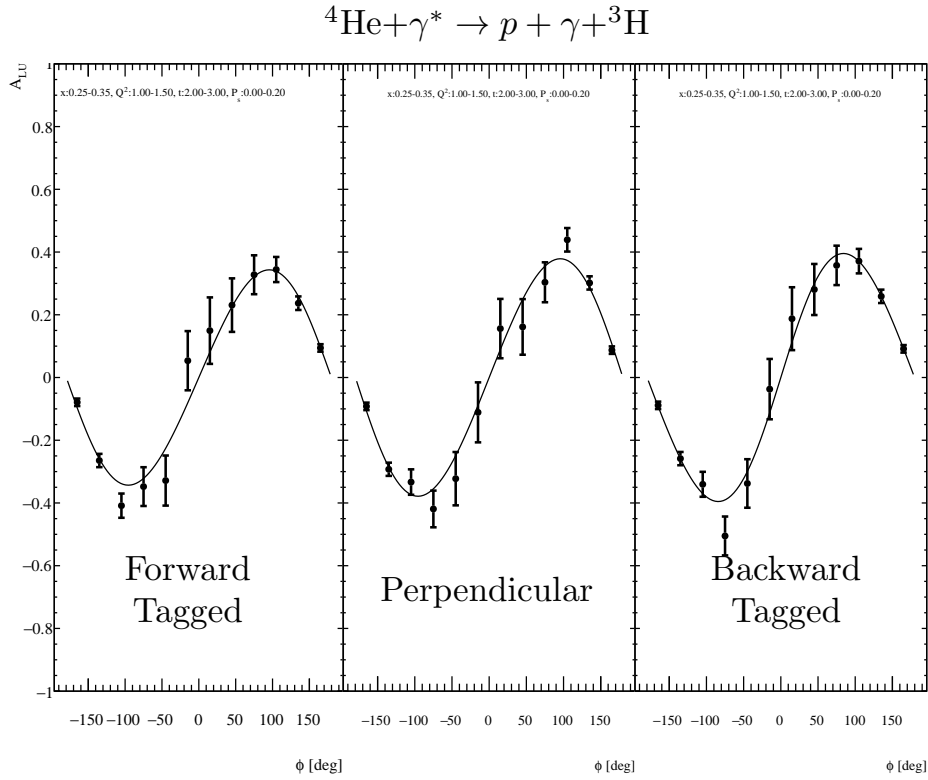


Figure 4.8: Expected statistical uncertainties on A_{LU} for three different bins in spectator angle, all corresponding to the lowest spectator momentum bin. The spectator angles are forward (left), perpendicular (center), and backward (right). Note the low momentum bin corresponds to the mean field nucleons.

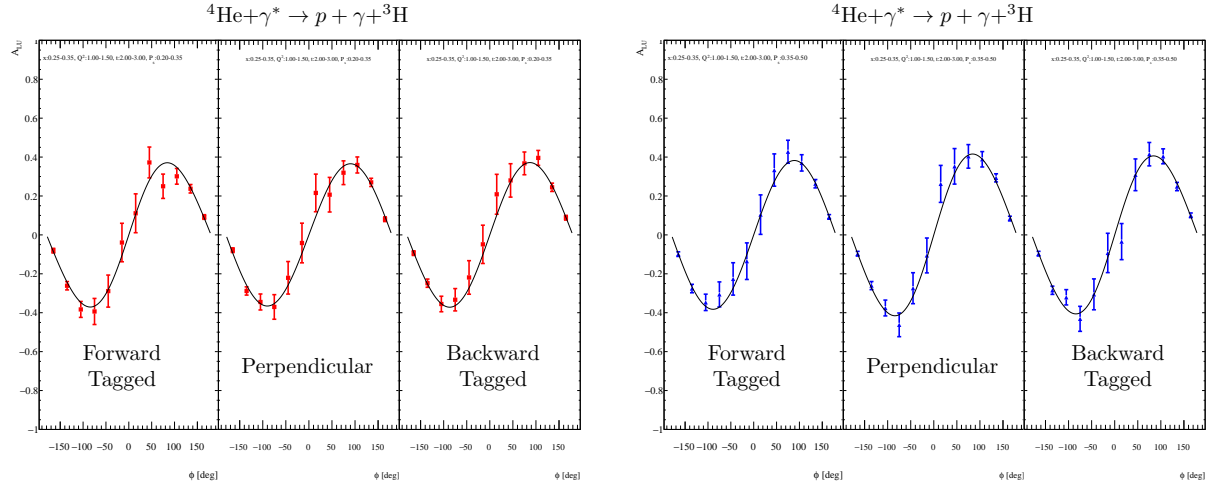


Figure 4.9: Expected statistical uncertainties of A_{LU} for θ_s bins identical to those in Fig. 4.8, but these results show the two higher spectator momentum bins. Note the highest momenta (blue) correspond to SRC nucleons.

spectators. We will match the kinematics where the FSI are observed to be negligible for the proton and look for nuclear effects in neutron. We define the following ratio for the extracted α values from DVCS on a quasi-free neutron in ^2H and from DVCS on a bound neutron in ^4He :

$$R_\alpha^N = \frac{\alpha_{N^*}^{(^4\text{He})}}{\alpha_N^{(^2\text{H})}} \quad (4.2)$$

where the N^* indicates the bound nucleon. We will identify nuclear effects by observing deviations from unity in this ratio and extracting its trend as function x , and for various spectator kinematics limits where we expect mean field nucleons or SRC nucleons to dominate. The projected statistical uncertainty is shown in Fig. 4.12.

4.3.2 Systematic Uncertainties

We estimate the main sources of systematic uncertainties from those ultimately obtained for the CLAS-eg6 experiment’s incoherent DVCS measurement [37]. They are listed in Table 4.2 along with our estimates for the beam spin asymmetry systematics. For the BSA the beam polarization will dominate our systematic uncertainties followed by the DVCS event selection cuts. With the significant improvement of ALERT for detecting the spectator recoils this uncertainty is expected to improve by more than a factor of two.

The so-called “acceptance ratio” corrects for the π^0 background and is defined for each bin as

$$R_{\pi^0} = \frac{N_{\pi(\gamma)}}{N_{\pi(\gamma\gamma)}} \quad (4.3)$$

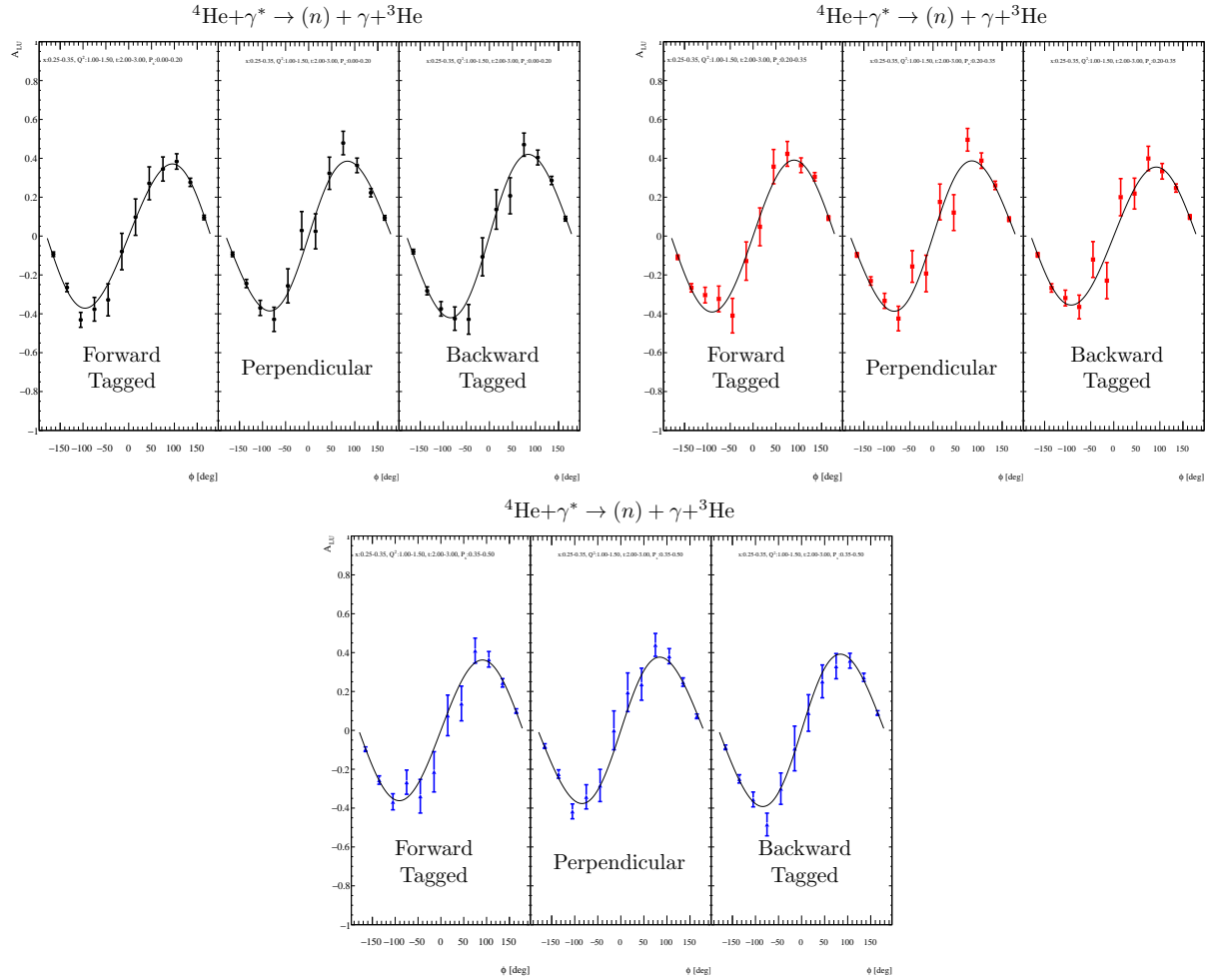


Figure 4.10: Expected statistical uncertainties of A_{LU} for θ_s bins identical to those in Fig. 4.8, but these results show the two higher spectator momentum bins. Note the lowest spectator momenta (black) are associated with mean field nucleons while the highest momenta (blue) correspond to SRC nucleons.

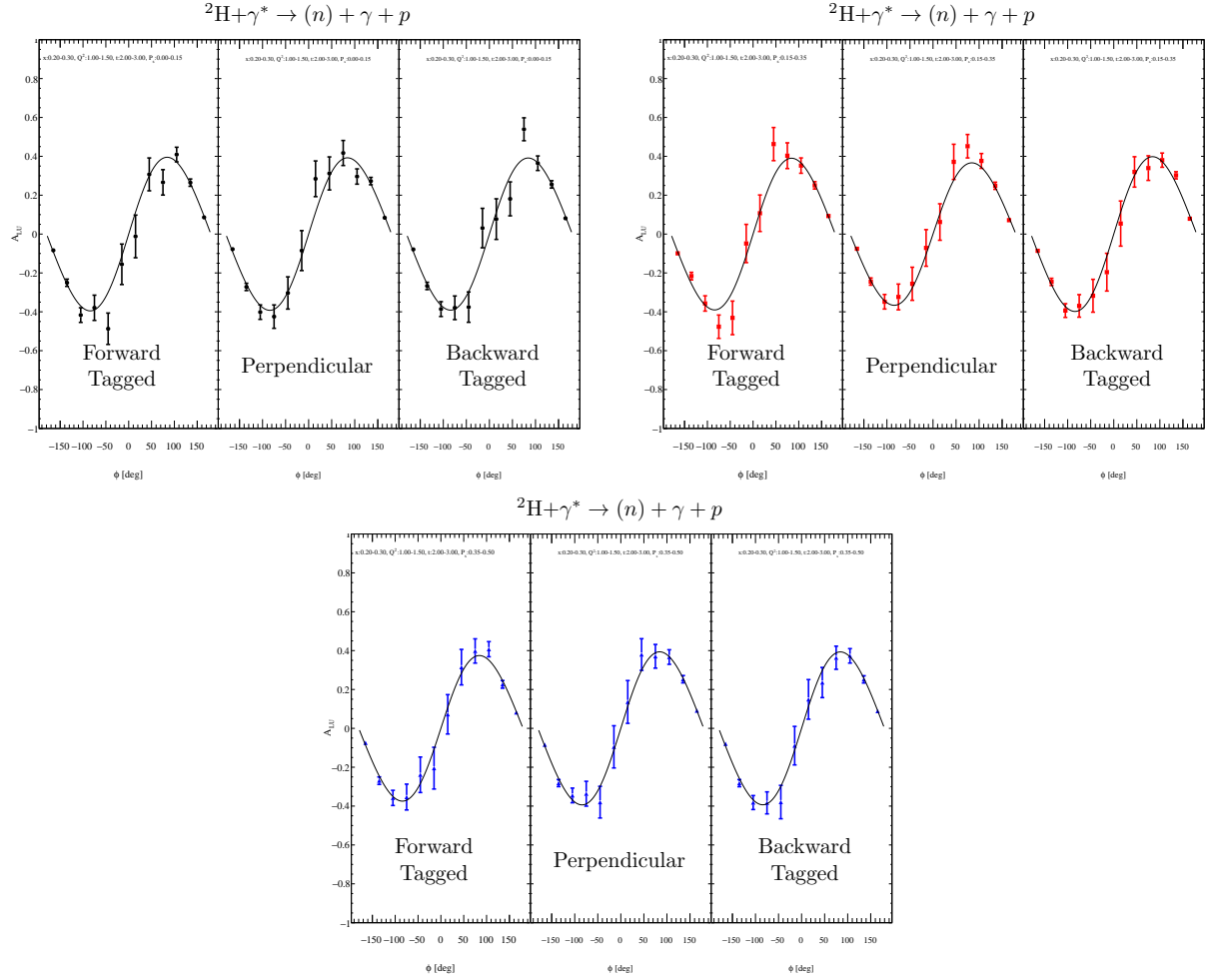


Figure 4.11: Projected statistical uncertainties of A_{LU} for θ_s bins identical to those in Fig. 4.8, but these results show the two higher spectator momentum bins. Note the lowest spectator momenta (black) are associated with mean field nucleons while the highest momenta (blue) correspond to SRC nucleons.

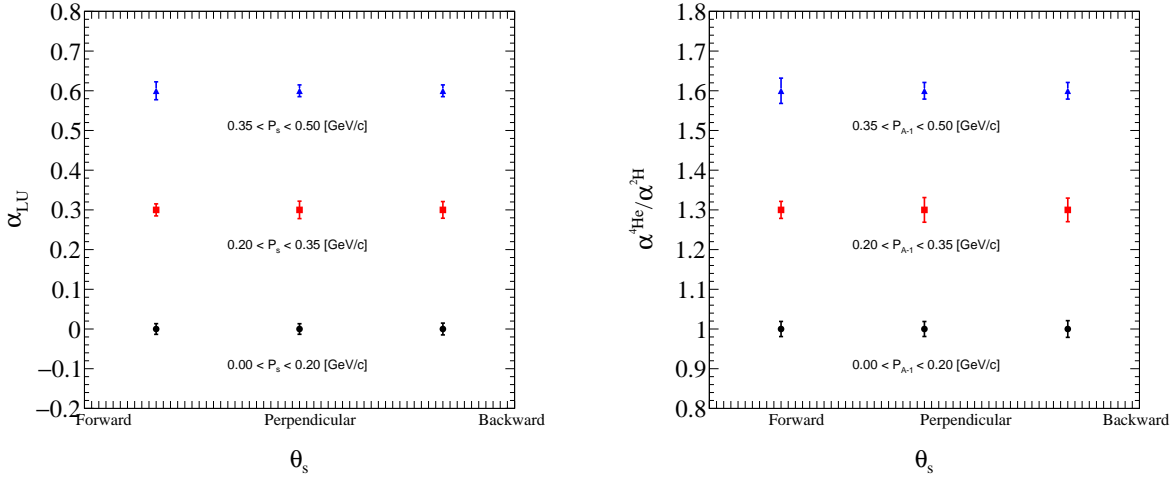


Figure 4.12: Left: Projected uncertainties after fitting the beam spin asymmetry with Equation 4.1 to the extract a value of α . Each t bin has 3 bins in P_{A-1} , which are offset vertically for clarity. Right: The ratio of α s for a bound neutron and a quasi-free nucleon.

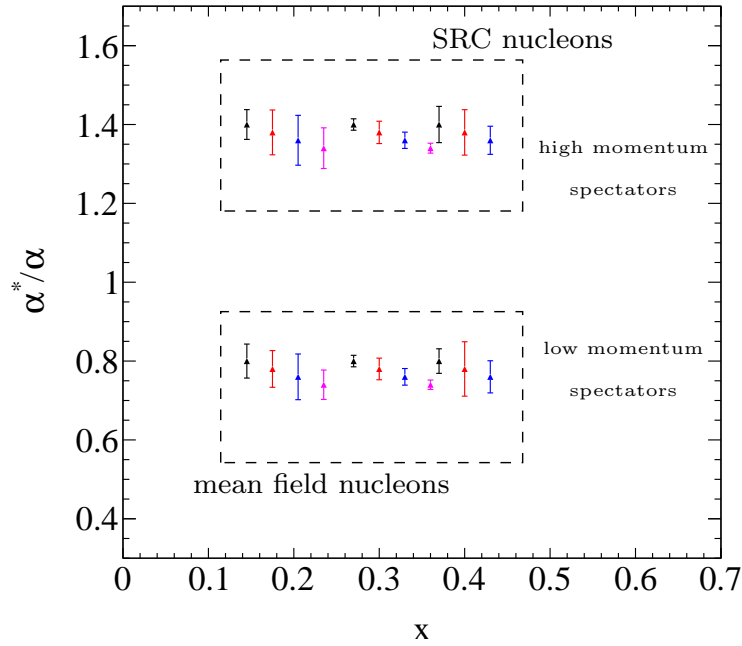


Figure 4.13: A subset of the R_α ratios for all Q^2 with backward tagged spectators. The highest spectator momenta bins are offset vertically above the lowest spectator momenta and the colors indicate the different t bins which are shifted horizontally for clarity.

Uncertainty source	CLAS-eg6	CLAS12 ALERT
Beam polarization	3.5%	3.5%
DVCS event selection	3.7%	1.0%
Acceptance ratio	2.0%	<1.0%
Others	0.1%	0.1%
Total	5.5%	4.0%

Table 4.2: Estimates of the expected systematic uncertainties compared to CLAS-eg6.

where $N_{\pi(\gamma)}$ and $N_{\pi(\gamma\gamma)}$ are the rates for exclusive electro-production of π^0 s where one decay photon is detected and where both decay photons are detected, respectively. The ratio calculated in Equation. 4.2 has the benefit that the acceptance cancels in the ratio under the approximation $R_{\pi^0}(^4\text{He}) \simeq R_{\pi^0}(^2\text{H})$.

Summary and Beam Time Request

Spectator tagged DVCS on ^2H and ^4He is of critical importance for two reasons. First and foremost, it identifies the active nucleon in the DVCS process. Secondly, spectator tagging provides a handle on the initial nucleon momenta, *i.e.*, it allows us to separate the mean field nucleons from the short range correlated nucleons. Tagged incoherent DVCS uniquely provides important leverage for identifying and isolating final state interactions while simultaneously probing the struck nucleon at the parton level. Furthermore, the neutron beam spin asymmetry is very sensitive to nuclear effects (see 1). Therefore cleanly extracting the neutron DVCS beam spin asymmetry, as we propose to do, in both bound and quasi-free configurations, will produce a *high impact result* from which we are able to *unambiguously* conclude that nucleons are modified in medium at the parton level. It also allows for the systematic control over FSI needed to conclusively observe, in isolation, mean field modified nucleons and SRC modified nucleons.

In order to achieve the uncertainties presented in this proposal, we need 20 days of running at 11 GeV with helium target, 20 days at 11 GeV with deuterium, both with 80% longitudinally polarized beam, and 5 days of commissioning of the ALERT detector at 11 GeV and 2.2 GeV (2.5 days each) with helium and hydrogen targets.

Relation to other experiments

This experiment will greatly complement many already approved experiments and previously conducted experiments.

First, the approved E12-11-003 experiment [48], “Deeply Virtual Compton Scattering on the Neutron with CLAS12 at 11 GeV” is set to measure the n-DVCS beam spin asymmetry by directly detecting the struck neutron in the reaction $\gamma^* + d \rightarrow n + \gamma + (p)$. While we intend to also measure the BSA through detection of the spectator proton instead, this is not the main thrust of this proposal. We aim to observe a medium modified neutron by also looking at a similar reaction on the neutron with a helium target where a spectator ^3He is detected.

The approved E12-06-113 experiment [19], “The Structure of the Free Neutron at Large x-Bjorken” will measure the neutron structure function in DIS through spectator tagging a recoil proton using the BoNuS12 detector. The reaction $e + d \rightarrow e + p_s + (X)$ is aimed at the deuteron’s quasi-free neutron, as is our DVCS BSA with a deuteron target. However, we also will investigate the bound neutron. Our main deliverable is the ratio of the BSA $\sin \phi$

harmonics from bound and quasi-free neutrons and it is a *model independent observable*.

Because we will study the FSIs through the fully detected final state, as highlighted throughout this proposal, we will be able to directly test the validity of the PWIA over a wide range of spectator kinematics. This information will directly benefit both experiments mentioned (and many more). The knowledge of the FSIs can be used to tune the models needed to extract the on-shell neutron structure function. Furthermore, the neutron DVCS observable will also be sensitive to FSIs which can be further understood with the results of this experiment.

Bibliography

- [1] S. Chekanov *et al.*, “Measurement of deeply virtual Compton scattering at HERA,” *Phys. Lett.*, vol. B573, pp. 46–62, 2003.
- [2] A. Aktas *et al.*, “Measurement of deeply virtual compton scattering at HERA,” *Eur. Phys. J.*, vol. C44, pp. 1–11, 2005.
- [3] C. M. Camacho *et al.*, “Scaling tests of the cross-section for deeply virtual compton scattering,” *Phys. Rev. Lett.*, vol. 97, p. 262002, 2006.
- [4] F. X. Girod *et al.*, “Measurement of Deeply virtual Compton scattering beam-spin asymmetries,” *Phys. Rev. Lett.*, vol. 100, p. 162002, 2008.
- [5] M. Mazouz *et al.*, “Deeply virtual compton scattering off the neutron,” *Phys. Rev. Lett.*, vol. 99, p. 242501, 2007.
- [6] M. M. Rvachev *et al.*, “The Quasielastic He-3(e,e’p)d reaction at $Q^{*2} = 1.5\text{-GeV}^{*2}$ for recoil momenta up to 1-GeV/c,” *Phys. Rev. Lett.*, vol. 94, p. 192302, 2005.
- [7] M. Paolone *et al.*, “Polarization Transfer in the 4He(e,e’p)3H Reaction at $Q^2 = 0.8$ and 1.3 (GeV/c)^2 ,” *Phys. Rev. Lett.*, vol. 105, p. 072001, 2010.
- [8] S. P. Malace *et al.*, “A precise extraction of the induced polarization in the 4He(e,e’p)3H reaction,” *Phys. Rev. Lett.*, vol. 106, p. 052501, 2011.
- [9] F. Sabatie *et al.*, “Deeply Virtual Compton Scattering with CLAS at 11 GeV,” *A proposal to PAC 30*, 2006.
- [10] C. Hyde *et al.*, “Measurements of Electron-Helicity Dependent Cross Sections of Deeply Virtual Compton Scattering with CEBAF at 12 GeV,” *A proposal to PAC 38*, 2011.
- [11] J. J. Aubert *et al.*, “The ratio of the nucleon structure functions $F2_n$ for iron and deuterium,” *Phys. Lett.*, vol. B123, pp. 275–278, 1983.
- [12] L. Weinstein *et al.*, “Short Range Correlations and the EMC Effect,” *Phys.Rev.Lett.*, vol. 106, p. 052301, 2011.

-
- [13] Z. E. Meziani *et al.*, “Coulomb Sum Rule for Ca-40, Ca-48, and Fe-56 for $|\vec{q}| \leq 550$ -MeV/c,” *Phys. Rev. Lett.*, vol. 52, pp. 2130–2133, 1984.
 - [14] J. Morgenstern and Z. E. Meziani, “Is the Coulomb sum rule violated in nuclei?,” *Phys. Lett.*, vol. B515, pp. 269–275, 2001.
 - [15] Cloët, Ian C. and Bentz, Wolfgang and Thomas, Anthony W., “Relativistic and Nuclear Medium Effects on the Coulomb Sum Rule,” *Phys. Rev. Lett.*, vol. 116, no. 3, p. 032701, 2016.
 - [16] C. Ciofi degli Atti and B. Z. Kopeliovich, “Final state interaction in semiinclusive DIS off nuclei,” *Eur. Phys. J.*, vol. A17, pp. 133–144, 2003.
 - [17] X.-D. Ji, “Gauge-Invariant Decomposition of Nucleon Spin,” *Phys. Rev. Lett.*, vol. 78, pp. 610–613, 1997.
 - [18] H. Fenker *et al.*, “BoNus: Development and use of a radial TPC using cylindrical GEMs,” *Nucl. Instrum. Meth.*, vol. A592, pp. 273–286, 2008.
 - [19] M. Amarian *et al.*, “The Structure of the Free Neutron at Large x-Bjorken (PR12-06-113),” *A proposal to PAC 30*, 2006.
 - [20] I. C. Cloet, W. Bentz, and A. W. Thomas, “Spin-dependent structure functions in nuclear matter and the polarized EMC effect,” *Phys. Rev. Lett.*, vol. 95, p. 052302, 2005.
 - [21] M. Burkardt, “Impact parameter space interpretation for generalized parton distributions,” *Int. J. Mod. Phys.*, vol. A18, pp. 173–208, 2003.
 - [22] V. Guzey, A. W. Thomas, and K. Tsushima, “Medium modifications of the bound nucleon GPDs and incoherent DVCS on nuclear targets,” *Phys. Lett.*, vol. B673, pp. 9–14, 2009.
 - [23] S. Liuti and S. K. Taneja, “Nuclear medium modifications of hadrons from generalized parton distributions,” *Phys. Rev.*, vol. C72, p. 034902, 2005.
 - [24] S. Liuti, “Connection between in medium nucleon form-factors and deep inelastic structure functions,” 2006.
 - [25] R. Dupre and S. Scopetta, “3D Structure and Nuclear Targets,” 2015.
 - [26] C. C. d. Atti, “In-medium short-range dynamics of nucleons: Recent theoretical and experimental advances,” *Phys. Rept.*, vol. 590, pp. 1–85, 2015.
 - [27] S. Jeschonnek and J. W. Van Orden, “A New calculation for D(e, e-prime p)n at GeV energies,” *Phys. Rev.*, vol. C78, p. 014007, 2008.

- [28] V. Guzey and M. Strikman, “DVCS on spinless nuclear targets in impulse approximation,” *Phys. Rev.*, vol. C68, p. 015204, 2003.
- [29] F. Cano and B. Pire, “Deep electroproduction of photons and mesons on the deuteron,” *Eur. Phys. J.*, vol. A19, pp. 423–438, 2004.
- [30] A. Kirchner and D. Mueller, “Deeply virtual Compton scattering off nuclei,” *Eur. Phys. J.*, vol. C32, pp. 347–375, 2003.
- [31] V. M. Braun, A. N. Manashov, D. Mueller, and B. Pirnay, “Resolving kinematic ambiguities in QCD predictions for Deeply Virtual Compton Scattering,” *PoS*, vol. DIS2014, p. 225, 2014.
- [32] A. V. Belitsky, D. Mueller, and A. Kirchner, “Theory of deeply virtual Compton scattering on the nucleon,” *Nucl. Phys.*, vol. B629, pp. 323–392, 2002.
- [33] A. V. Belitsky and D. Mueller, “Exclusive electroproduction revisited: treating kinematical effects,” *Phys. Rev.*, vol. D82, p. 074010, 2010.
- [34] Belitsky, Andrei V. and Müller, Dieter and Ji, Yao, “Compton scattering: from deeply virtual to quasi-real,” *Nucl. Phys.*, vol. B878, pp. 214–268, 2014.
- [35] A. V. Belitsky, D. Mueller, L. Niedermeier, and A. Schafer, “Leading twist asymmetries in deeply virtual Compton scattering,” *Nucl. Phys.*, vol. B593, pp. 289–310, 2001.
- [36] M. Guidal, H. Moutarde, and M. Vanderhaeghen, “Generalized Parton Distributions in the valence region from Deeply Virtual Compton Scattering,” *Rept. Prog. Phys.*, vol. 76, p. 066202, 2013.
- [37] M. Hattawy *et al.* (EG6 Working Group), “Deeply Virtual Compton Scattering off ^4He ,” *CLAS internal analysis note*, 2016.
- [38] S. Liuti and S. K. Taneja, “Microscopic description of deeply virtual Compton scattering off spin-0 nuclei,” *Phys. Rev.*, vol. C72, p. 032201, 2005.
- [39] R. B. Wiringa, R. Schiavilla, S. C. Pieper, and J. Carlson, “Nucleon and nucleon-pair momentum distributions in $A \leq 12$ nuclei,” *Phys. Rev.*, vol. C89, no. 2, p. 024305, 2014.
- [40] “CLAS12 Technical Design Report,” 2008.
- [41] J. Peyré, B. Genolini, and J. Poutas, “A Full-Scale Prototype for the Tracking Chambers of the ALICE Muon Spectrometer,” 1998.
- [42] T. Abe *et al.*, “Belle II Technical Design Report,” 2010.
- [43] E. Etzion *et al.*, “The Certification of ATLAS Thin Gap Chambers Produced in Israel and China,” 2004.

- [44] S. Biagi, “Monte Carlo simulation of electron drift and diffusion in counting gases under the influence of electric and magnetic fields,” *Nucl.Instrum.Meth.*, vol. A421, pp. 234–240, 1999.
- [45] M. Battaglieri *et al.*, “The Heavy Photon Search test detector,” *Nucl.Instrum.Meth.*, vol. A777, pp. 91–101, 2015.
- [46] T. C. Collaboration, “Clas12 forward tagger (ft) technical design report.” <https://www.jlab.org/Hall-B/clas12-web/docs/ft-tdr.2.0.pdf>, 2012. Online; accessed 29 January 2016.
- [47] K. Emi *et al.*, “Study of a dE/dx measurement and the gas-gain saturation by a prototype drift chamber for the BELLE-CDC,” *Nucl. Instrum. Meth.*, vol. A379, pp. 225–231, 1996.
- [48] S. Niccolai *et al.*, “Deeply Virtual Compton Scattering on the Neutron with CLAS12 at 11 GeV,” *A proposal to PAC 38*, 2011.
- [49] M. Diehl, “Generalized parton distributions with helicity flip,” *Eur. Phys. J.*, vol. C19, pp. 485–492, 2001.
- [50] X.-D. Ji, “Off forward parton distributions,” *J. Phys.*, vol. G24, pp. 1181–1205, 1998.
- [51] A. V. Radyushkin, “Nonforward parton distributions,” *Phys. Rev.*, vol. D56, pp. 5524–5557, 1997.
- [52] K. Goeke, M. V. Polyakov, and M. Vanderhaeghen, “Hard exclusive reactions and the structure of hadrons,” *Prog. Part. Nucl. Phys.*, vol. 47, pp. 401–515, 2001.
- [53] P. Hoodbhoy and X. Ji, “Helicity-flip off-forward parton distributions of the nucleon,” *Phys. Rev. D*, vol. 58, p. 054006, Jul 1998.
- [54] M. Diehl, “Generalized parton distributions,” *Phys. Rept.*, vol. 388, pp. 41–277, 2003.
- [55] V. Bernard, N. Kaiser, and U.-G. Meissner, “Nucleon electroweak form-factors: Analysis of their spectral functions,” *Nucl. Phys.*, vol. A611, pp. 429–441, 1996.
- [56] A. Belitsky and A. Radyushkin, “Unraveling hadron structure with generalized parton distributions,” *Physics Reports*, vol. 418, pp. 1–387, 10 2005.
- [57] L. Mankiewicz, G. Piller, and T. Weigl, “Hard exclusive meson production and nonforward parton distributions,” *Eur. Phys. J.*, vol. C5, pp. 119–128, 1998.
- [58] X. Ji, “Deeply virtual compton scattering,” *Phys. Rev. D*, vol. 55, pp. 7114–7125, Jun 1997.

-
- [59] J. Ashman *et al.*, “An Investigation of the Spin Structure of the Proton in Deep Inelastic Scattering of Polarized Muons on Polarized Protons,” *Nucl. Phys.*, vol. B328, p. 1, 1989.
- [60] C. Lorce, “Geometrical approach to the proton spin decomposition,” *Phys. Rev.*, vol. D87, no. 3, p. 034031, 2013.
- [61] A. V. Belitsky and D. Müller, “Exclusive electroproduction revisited: Treating kinematical effects,” *Phys. Rev. D*, vol. 82, p. 074010, Oct 2010.

Appendix A

DVCS Formalism

A.1 Theory bound nucleon DVCS

In the infinite-momentum frame, where the initial and the final nucleons go at the speed of light along the positive z-axis, the partons have relatively small transverse momenta compared to their longitudinal momenta. Referring to figure A.1, the struck parton carries a longitudinal momentum fraction $x + \xi$ and it goes back into the nucleon with a momentum fraction $x - \xi$. The GPDs are defined in the interval where x and $\xi \in [-1,1]$, which can be separated into three regions as can be seen in figure A.1. The regions are:

- $x \in [\xi, 1]$: both momentum fractions $x + \xi$ and $x - \xi$ are positive and the process describes the emission and reabsorption of a quark.
- $x \in [-\xi, \xi]$: $x + \xi$ is positive reflecting the emission of a quark, while $x - \xi$ is negative and is interpreted as an antiquark being emitted from the initial proton.
- $x \in [-1, -\xi]$: both fractions are negative, and $x + \xi$ and $x - \xi$ represent the emission and reabsorption of antiquarks.

The GPDs in the first and in the third regions represent the probability amplitude of finding a quark or an antiquark in the nucleon, while in the second region they represent the probability amplitude of finding a quark-antiquark pair in the nucleon [49].

Following the definition of reference [50], the differential DVCS cross section is obtained from the DVCS scattering amplitude (\mathcal{T}_{DVCS}) as:

$$\frac{d^5\sigma}{dQ^2 dx_B dt d\phi d\phi_e} = \frac{1}{(2\pi^4)32} \frac{x_B y^2}{Q^4} \left(1 + \frac{4M^2 x_B^2}{Q^2}\right)^{-1/2} |\mathcal{T}_{DVCS}|^2, \quad (\text{A.1})$$

where ϕ_e is the azimuthal angle of the scattered lepton, $y = \frac{E-E'}{E}$ and Q^2, x_B, t, ϕ are the four kinematic variables that describe the process. The variable ϕ is the angle

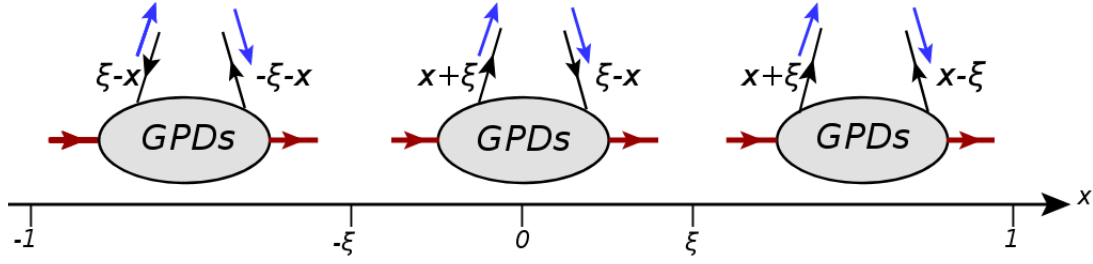


Figure A.1: The parton interpretations of the GPDs in three x -intervals $[-1, -\xi]$, $[-\xi, \xi]$ and $[\xi, 1]$. The red arrows indicate the initial and the final-state of the proton, while the blue (black) arrows represent helicity (momentum) of the struck quark.

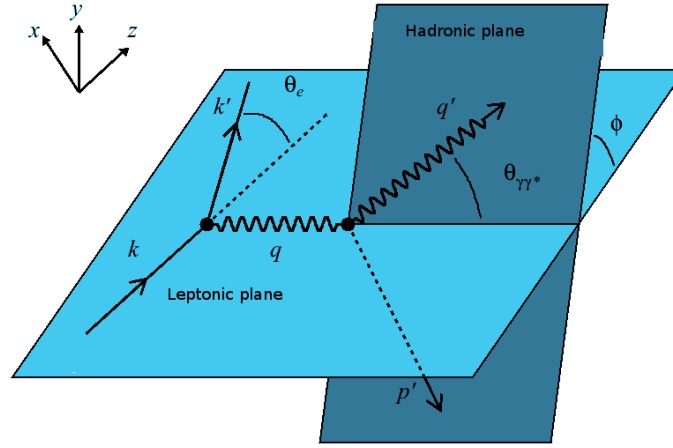


Figure A.2: The definition of the azimuthal angle ϕ between the leptonic and the hadronic planes.

between the leptonic and the hadronic planes, as can be seen in figure A.2.

By neglecting the mass of the quark with respect to the energies of γ^* and γ , the DVCS scattering amplitude can be parametrized by four quark helicity conserving (chiral-even)

GPDs: H , E , \tilde{H} and \tilde{E} as:

$$\mathcal{T}_{DVCS} = \sum_q (|e|Q_q)^2 \varepsilon_\mu^* \varepsilon_\nu \left\{ \begin{aligned} & g_\perp^{\mu\nu} \int_{-1}^1 dx \left[\frac{1}{x - \xi + i\varepsilon} + \frac{1}{x + \xi - i\varepsilon} \right] \times \frac{1}{2} \bar{u}(p') \left[H^q \gamma^+ + E^q i\sigma^{+\alpha} \frac{\Delta_\alpha}{2m_N} \right] u(p) \\ & + i\varepsilon^{\mu\nu+-} \int_{-1}^1 dx \left[\frac{1}{x + \xi - i\varepsilon} - \frac{1}{x - \xi + i\varepsilon} \right] \times \frac{1}{2} \bar{u}(p') \left[\tilde{H}^q \gamma^+ \gamma_5 + \tilde{E}^q \gamma_5 \frac{\Delta^+}{2m_N} \right] u(p) \end{aligned} \right\}, \quad (\text{A.2})$$

where $\bar{u}(p')$ and $u(p)$ are the spinors of the nucleon.

The GPDs H , E , \tilde{H} and \tilde{E} are defined for each quark flavor ($q = u, d, s, \dots$). Analogous GPDs exist for the gluons, see references [51, 50, 52] for details. In this work, we are mostly concerned by the valence quark region, in which the sea quarks and the gluons contributions do not dominate the DVCS scattering amplitude.

The GPDs H , E , \tilde{H} and \tilde{E} are called chiral-even GPDs because they conserve the helicity of the struck quark. The GPDs H and \tilde{H} conserve the spin of the nucleon, while E and \tilde{E} flip it. The H and E GPDs are called the unpolarized GPDs as they represent the sum over the different configurations of the quarks' helicities, whereas \tilde{H} and \tilde{E} are called the polarized GPDs because they are made up of the difference between the orientations of the quarks' helicities.

If one keeps the quark mass, another set of GPDs gives contribution to the DVCS amplitude. They are called chiral-odd GPDs. They give information about the quarks helicity-flip transitions. At leading twist, there are four chiral-odd GPDs that parametrize the helicity-flip structure of the partons in a nucleon: H_T , E_T , \tilde{H}_T and \tilde{E}_T [53]. Analogous set of chiral-odd GPDs exist for the gluon sector (see [53, 54]). The chiral-even GPDs contribute mostly in the regions where $\xi < x$ and $x < -\xi$, while the chiral-odd GPDs have larger contribution in the $x < |\xi|$ region [50].

A.1.0.1 Basic properties of GPDs

Links to the ordinary FFs and PDFs Links between GPDs and the FFs are constructed by integrating the GPDs over the momentum fraction x at given momentum transfer (t). Because of Lorentz invariance, integrating over x removes all the references to the particular light-cone frame, in which ξ is defined. Therefore, the result must be ξ -independent as can

be see in equation A.3:

$$\begin{aligned} \int_{-1}^1 dx H^q(x, \xi, t) &= F_1^q(t), & \int_{-1}^1 dx E^q(x, \xi, t) &= F_2^q(t), \\ \int_{-1}^1 dx \tilde{H}^q(x, \xi, t) &= G_A^q(t), & \int_{-1}^1 dx \tilde{E}^q(x, \xi, t) &= G_P^q(t), \end{aligned} \quad (\text{A.3})$$

where $F_1^q(t)$ and $F_2^q(t)$ are the previously introduced Dirac and Pauli FFs, $G_A^q(t)$ and $G_P^q(t)$ are the axial and pseudoscalar electroweak FFs. The latter two can be measured in electroweak interactions; see reference [55] for more details about the electroweak FFs.

From the optical theorem, the DIS cross section is proportional to the imaginary part of the forward amplitude of the doubly virtual Compton scattering (production of a spacelike ($Q^2 < 0$) virtual photon in the final state instead of a real photon) [36]. In the limit $\xi \rightarrow 0$ and $t \rightarrow 0$, the GPDs are reduced to the ordinary PDFs, such that for the quark sector:

$$H^q(x, 0, 0) = q(x), \quad \tilde{H}^q(x, 0, 0) = \Delta q(x), \quad (\text{A.4})$$

where $q(x)$ is the unpolarized PDF, defined for each quark flavor. The polarized PDFs $\Delta q(x)$ are accessible from polarized-beam and polarized-target DIS experiments. There are no similar relations for the GPDs E and \tilde{E} , as in the scattering amplitude, equation A.2, they are multiplied by factors proportional to t ($= \Delta^2$), which vanish in the forward limit. Figure A.3 summarizes the physics interpretations of the GPDs, the FFs, the PDFs, and the links between them.

Polynomiality of GPDs The GPDs have a key property which is the polynomiality. This property comes from the Lorentz invariance of the nucleon matrix elements. It states that the x^n moment of the GPDs must be a polynomial in ξ with a maximum order of $n+1$ [50].

$$\int_{-1}^1 dx x^n H^q(x, \xi, t) = \sum_{(even)i=0}^n (2\xi)^i A_{n+1,i}^q(t) + mod(n, 2)(2\xi)^{n+1} C_{n+1}^q(t), \quad (\text{A.5})$$

$$\int_{-1}^1 dx x^n E^q(x, \xi, t) = \sum_{(even)i=0}^n (2\xi)^i B_{n+1,i}^q(t) - mod(n, 2)(2\xi)^{n+1} C_{n+1}^q(t), \quad (\text{A.6})$$

$$\int_{-1}^1 dx x^n \tilde{H}^q(x, \xi, t) = \sum_{(even)i=0}^n (2\xi)^i \tilde{A}_{n+1,i}^q(t), \quad (\text{A.7})$$

$$\int_{-1}^1 dx x^n \tilde{E}^q(x, \xi, t) = \sum_{(even)i=0}^n (2\xi)^i \tilde{B}_{n+1,i}^q(t). \quad (\text{A.8})$$

where $mod(n, 2)$ is 1 for odd n and 0 for even n . Thus, the corresponding polynomials contain only even powers of the skewedness parameter ξ . This follows from time-reversal

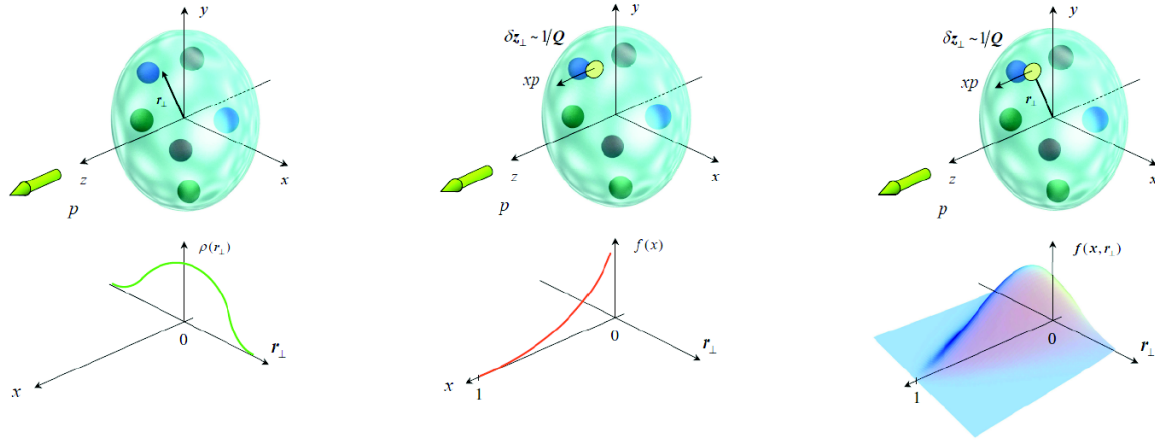


Figure A.3: The links between the GPDs and the ordinary FFs and PDFs. From left to right: the FFs reflect, via a Fourier transform, the two-dimensional spatial distributions of the quarks in the transverse plane; the PDFs give information about the longitudinal momentum distributions of the partons; finally, the GPDs provide a three-dimensional imaging of the partons in terms of both their longitudinal momenta and their position in the transverse space plane. The figure is from [56].

invariance, i.e. $GPD(x, \xi, t) = GPD(x, -\xi, t)$ [57]. This implies that the highest power of ξ is $n + 1$ for odd n (singlet GPDs) and of highest power n in case of even n (non-singlet GPDs). Due to the fact that the nucleon has spin $1/2$, the coefficients in front of the highest power of ξ for the singlet functions H^q and E^q are equal and have opposite signs. This sum rule is the same for the gluons [54].

As a consequence of the polynomiality of the GPDs, the first moments of GPDs lead to the ordinary form factors, as shown previously in this section. X. Ji derived a sum rule [58] that links the second moments of the quark GPDs H^q and E^q , in the forward limit ($t = 0$), to the total angular momentum ($J_{quarks} = \frac{1}{2}\Delta\Sigma + L_{quarks}$), where $\Delta\Sigma$ is the contribution of the quark spin to the nucleon spin and L_{quarks} is the quarks orbital angular momentum contribution, as:

$$J_{quarks} = \frac{1}{2} \int_{-1}^1 dx \, x [H^q(x, \xi, t = 0) + E^q(x, \xi, t = 0)] \quad (\text{A.9})$$

A similar expression exists for the gluons contribution (J_{gluons}).

The spin of a nucleon is built from the sum of the quarks' and the gluons' total angular momenta, $\frac{1}{2} = J_{quarks} + J_{gluons}$. Regarding the experimental measurements, the EMC collaboration [59] has measured the contribution of the spins of the quarks ($\Delta\Sigma$) to the nucleon spin to be around 30%. Therefore, measuring the second moments of the GPDs H and E will give access to the quarks orbital momentum (L_{quarks}) which will complete the sector

of the quarks in understanding the nucleon spin. For the gluon total angular momentum (J_{gluons}), it is still an open question how to decompose J_{gluons} into orbital (L_{gluons}) and spin (Δg) components and to access them experimentally, see reference [60] for more discussions on this subject.

A.1.0.2 Compton form factors

The GPDs are real functions of two experimentally measurable variables, ξ and t , and one unmeasurable variable, x , in the DVCS reaction. Therefore, the GPDs are not directly measurable. In DVCS what we measure are the Compton Form Factors (CFFs) that are linked to the GPDs. As shown in equation A.2, the DVCS scattering amplitude, at leading order in α_s and leading twist, contains x -integrals of the form, $\int_{-1}^{+1} dx \frac{GPD^q(x, \xi, t)}{x \pm \xi \mp i\epsilon}$, where $\frac{1}{x \pm \xi \mp i\epsilon}$ is the propagator of the quark between the two photons. The integrals can be written as:

$$\int_{-1}^{+1} dx \frac{GPD^q(x, \xi, t)}{x \pm \xi \mp i\epsilon} = \mathcal{P} \int_{-1}^{+1} dx \frac{GPD^q(x, \xi, t)}{x \pm \xi} \pm i\pi GPD^q(x = \mp \xi, \xi, t), \quad (\text{A.10})$$

where \mathcal{P} stands for the Cauchy principal value integral. The DVCS amplitude can be decomposed into four complex CFFs, such that for each GPD there is a corresponding CFF. For instance, for the GPD $H^q(x, \xi, t)$, the real and imaginary parts of its CFF ($\mathcal{H}(\xi, t)$) at leading order in α_s can be expressed as:

$$\mathcal{H}(\xi, t) = \Re(\mathcal{H})(\xi, t) - i\pi \Im(\mathcal{H})(\xi, t) \quad (\text{A.11a})$$

$$\text{with} \quad \Re(\mathcal{H})(\xi, t) = \mathcal{P} \int_0^1 dx [H(x, \xi, t) - H(-x, \xi, t)] C^+(x, \xi) \quad (\text{A.11b})$$

$$\text{and} \quad \Im(\mathcal{H})(\xi, t) = H(\xi, \xi, t) - H(-\xi, \xi, t), \quad (\text{A.11c})$$

where the term corresponding to the real part is weighted by $C^+(x, \xi) (= \frac{1}{x-\xi} + \frac{1}{x+\xi})$, which appears also in an analogous expression for the GPD $E^q(x, \xi, t)$. The real parts of the CFFs that are associated with the GPDs $\tilde{H}^q(x, \xi, t)$ and $\tilde{E}^q(x, \xi, t)$, are weighted by $C^-(x, \xi) (= \frac{1}{x-\xi} - \frac{1}{x+\xi})$.

A.1.0.3 Bethe-Heitler

Experimentally, the DVCS is indistinguishable from the Bethe-Heitler (BH) process, which is the reaction where the final photon is emitted either from the incoming or the outgoing leptons, as shown in figure A.4. The BH process is not sensitive to GPDs and does not carry information about the partonic structure of the hadronic target. The BH cross section is calculable from the well-known electromagnetic FFs.

The $ep \rightarrow ep\gamma$ differential cross section of a longitudinally-polarized electron beam on an

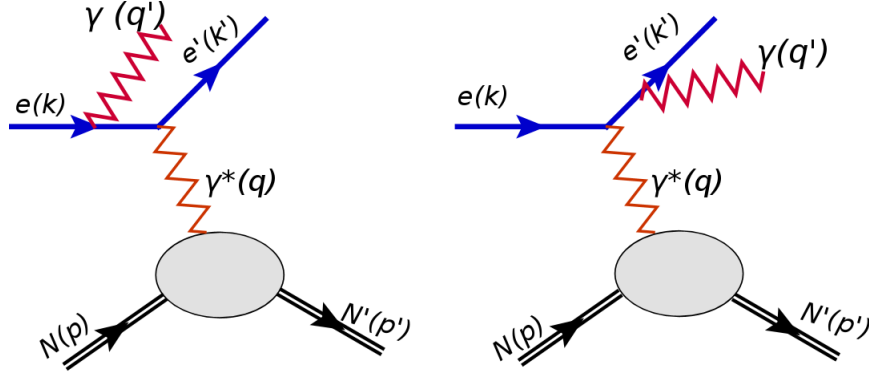


Figure A.4: Schematic for the Bethe-Heitler process. The final real photon can be emitted from the incoming electron (left plot) or from the scattered electron (right plot).

unpolarized proton target can be written as [61]:

$$\frac{d^5\sigma^\lambda}{dQ^2 dx_B dt d\phi d\phi_e} = \frac{\alpha^3}{16\pi^2} \frac{x_B y^2}{Q^2 \sqrt{1 + (2x_b M_N/Q)^2}} \frac{|\mathcal{T}_{BH}|^2 + |\mathcal{T}_{DVCS}^\lambda|^2 + \mathcal{I}_{BH*DVCS}^\lambda}{e^6} \quad (\text{A.12})$$

where λ is the beam helicity, \mathcal{T}_{DVCS} is the pure DVCS scattering amplitude, \mathcal{T}_{BH} is the pure BH amplitude and $\mathcal{I}_{BH*DVCS}^\lambda$ represents the interference amplitude. At leading twist, A. V. Belitsky, D. Mueller and A. Kirchner have shown that these amplitudes can be decomposed into a finite sum of Fourier harmonics, the so-called BMK formalism [61], as:

$$|\mathcal{T}_{BH}|^2 = \frac{e^6(1+\varepsilon^2)^{-2}}{x_B^2 y^2 t \mathcal{P}_1(\phi) \mathcal{P}_2(\phi)} \left[c_0^{BH} + \sum_{n=1}^2 \left(c_n^{BH} \cos(n\phi) + s_n^{BH} \sin(\phi) \right) \right] \quad (\text{A.13})$$

$$|\mathcal{T}_{DVCS}|^2 = \frac{e^6}{y^2 Q^2} \left[c_0^{DVCS} + \sum_{n=1}^2 \left(c_n^{DVCS} \cos(n\phi) + \lambda s_n^{DVCS} \sin(n\phi) \right) \right] \quad (\text{A.14})$$

$$\mathcal{I}_{BH*DVCS} = \frac{\pm e^6}{x_B y^3 t \mathcal{P}_1(\phi) \mathcal{P}_2(\phi)} \left[c_0^I + \sum_{n=0}^3 \left(c_n^I \cos(n\phi) + \lambda s_n^I \sin(n\phi) \right) \right] \quad (\text{A.15})$$

where $\mathcal{P}_1(\phi)$ and $\mathcal{P}_2(\phi)$ are the BH propagators. The leading twist expressions of the DVCS, BH and interference Fourier coefficients on a proton target can be found in reference [61]. The $+$ ($-$) sign in the interference term stands for the negatively (positively) charged lepton beam. In the case of an unpolarized proton target, the coefficients of the $\sin(\phi)$ in the BH amplitude are zeros.

Appendix B

Detailed Experimental Projections

B.1 Kinematic Coverage

Here we present many kinematic plots for the tagged DVCS reactions.

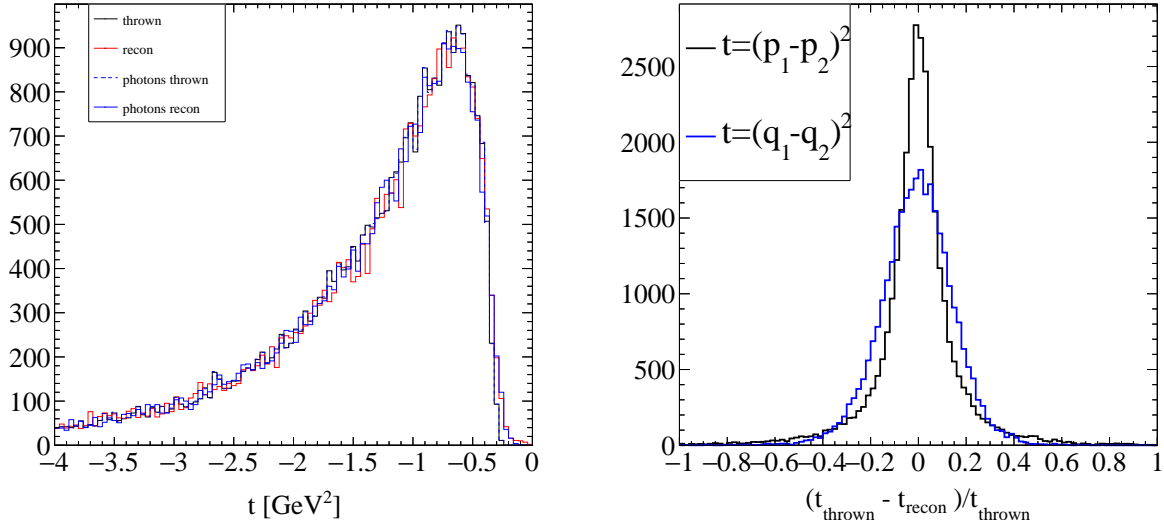


Figure B.1: Left: Thrown and reconstructed t calculated from the photons (t_q) and hadrons (t_p). Right: The corresponding resolutions for the two methods of determining t .

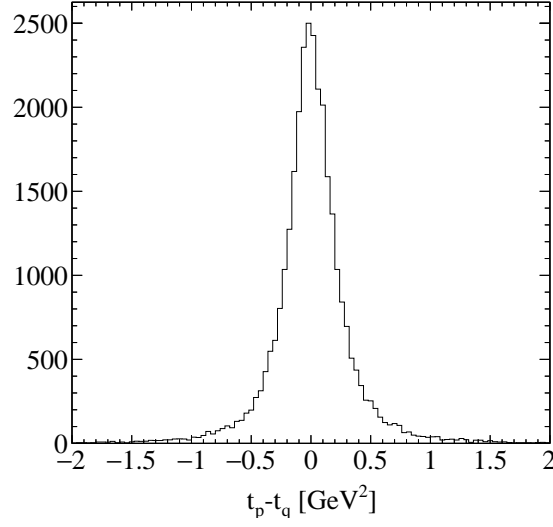


Figure B.2: The difference in the momentum transfers, $\delta t = t_p - t_q$.

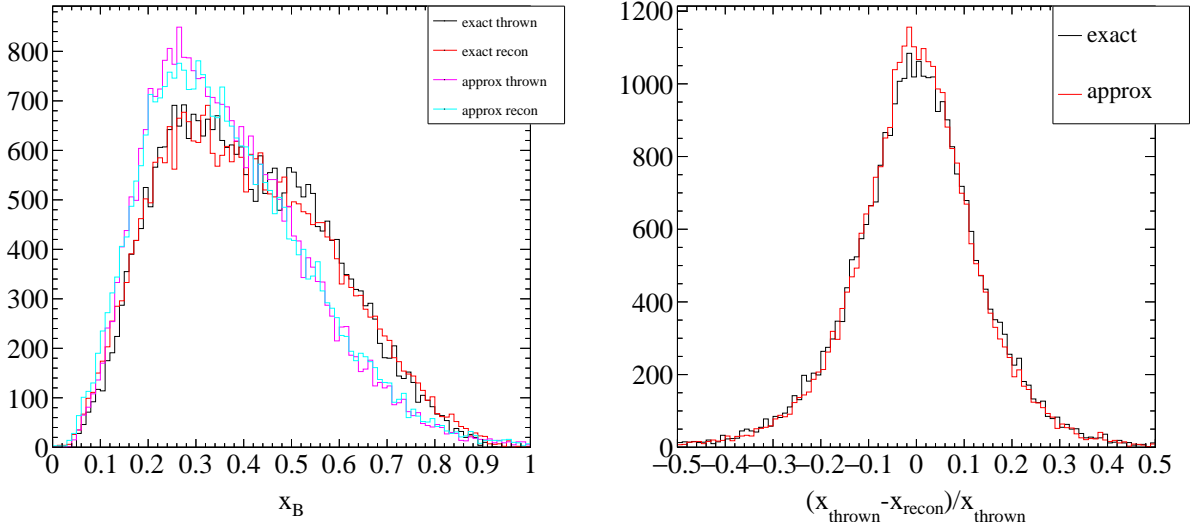
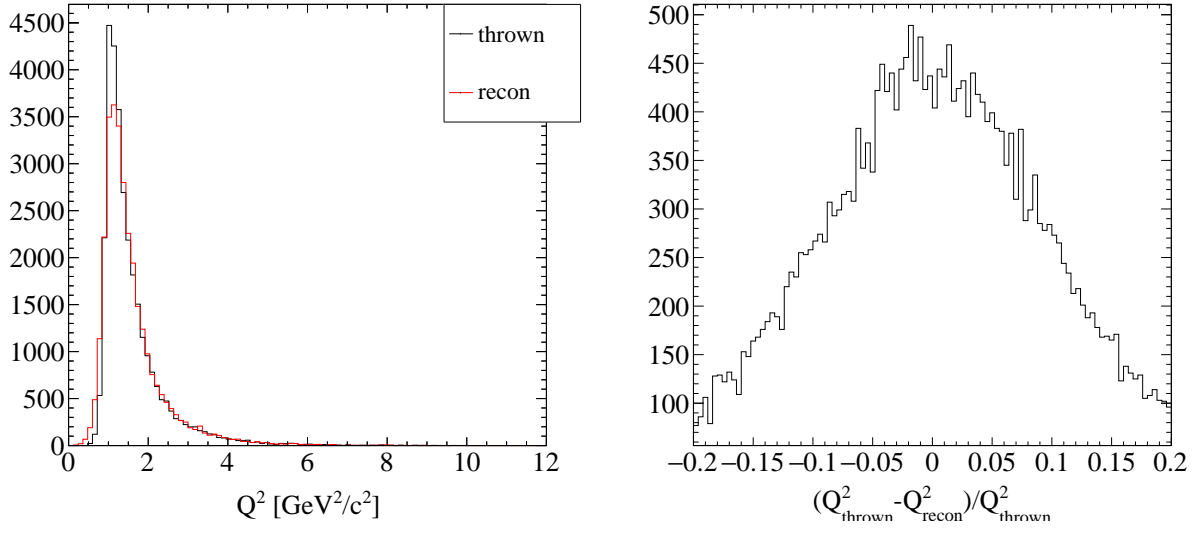
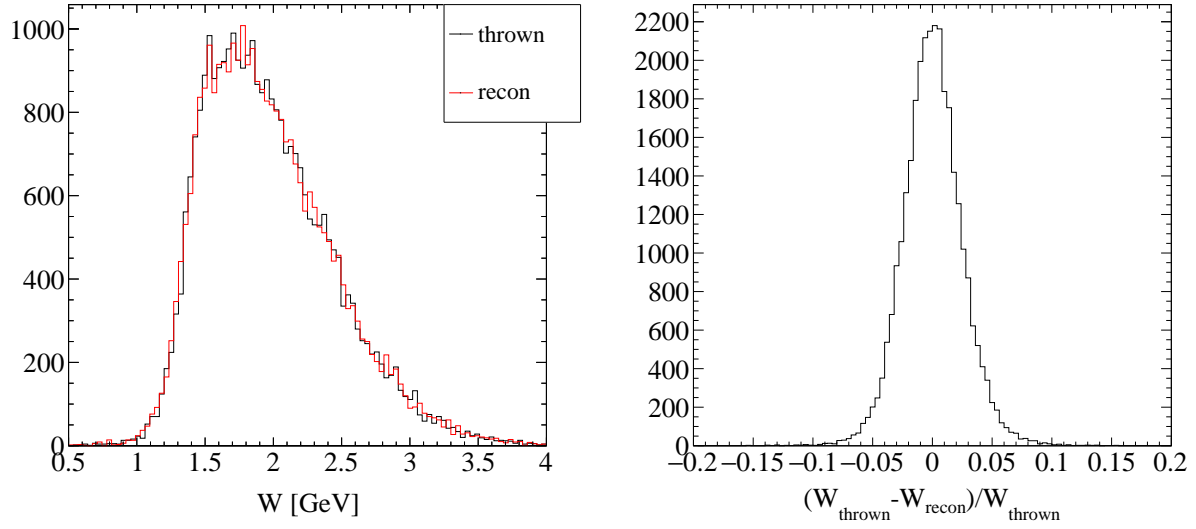


Figure B.3: Left: Thrown and reconstructed x_B where the approximate calculation assumes the struck nucleon is at rest, i.e., $x_{approx} = Q^2/2M\nu$. Right: Relative resolutions expected.

Figure B.4: Reconstructed Q^2 and its simulated resolution.Figure B.5: Reconstructed W and its simulated resolution.

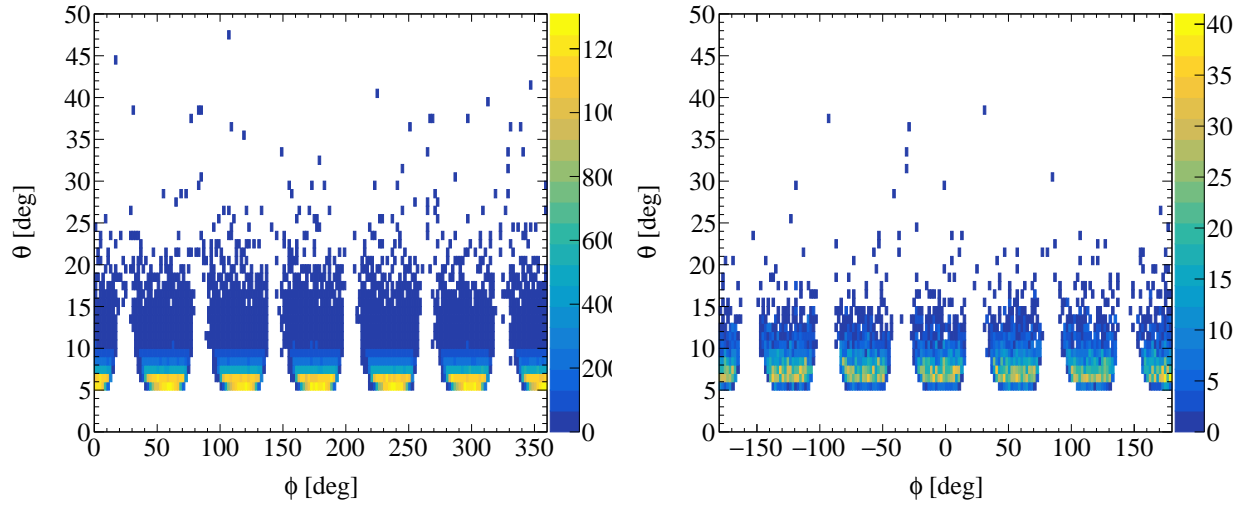


Figure B.6: Electron θ Vs. ϕ , before (left) and after (right) cuts.

B.2 Projections for $\sin\phi$ harmonic of the BSA

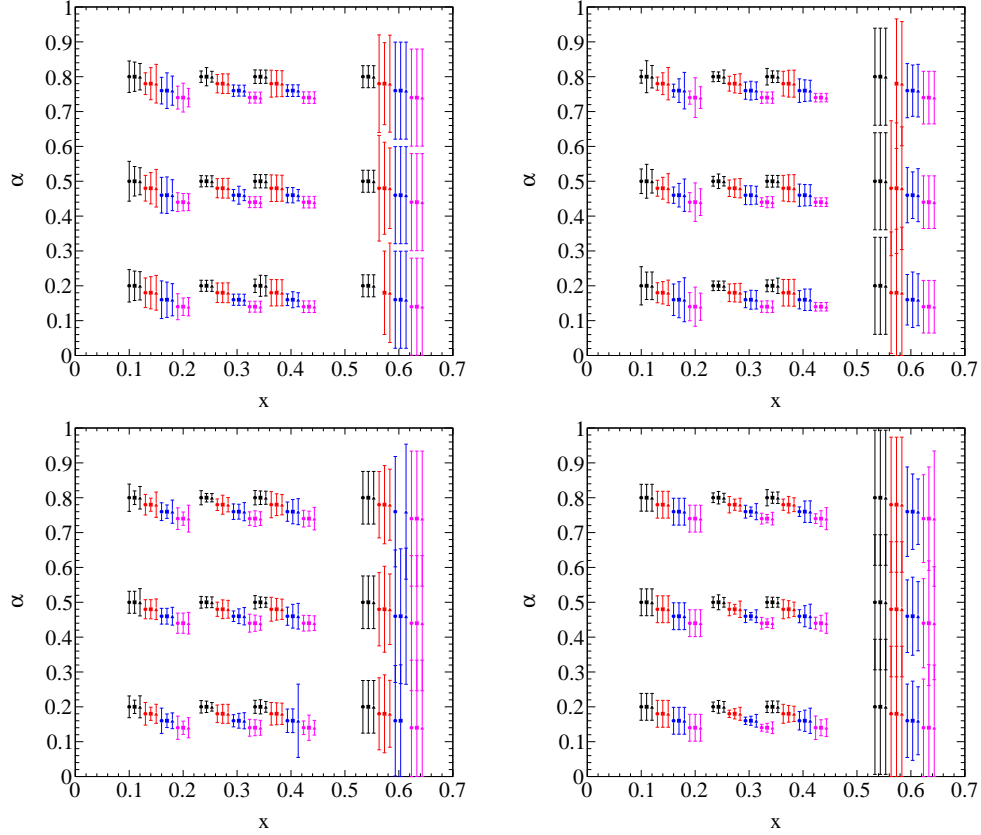


Figure B.7: Projected statistical uncertainty for the n-DVCS α from a ^4He target. The points are offset for clarity. Each plot shows the results for different Q^2 bins starting with the lowest in the upper left and the highest in the lower right. The horizontal bands of points starting from low to high are for the three spectator momentum bins (like Fig. 4.12) and the different symbols indicate the spectator angle bins. The points color along with points grouped with a slight negative slope are for different t bins starting with black for the lows $|t|$ bin.

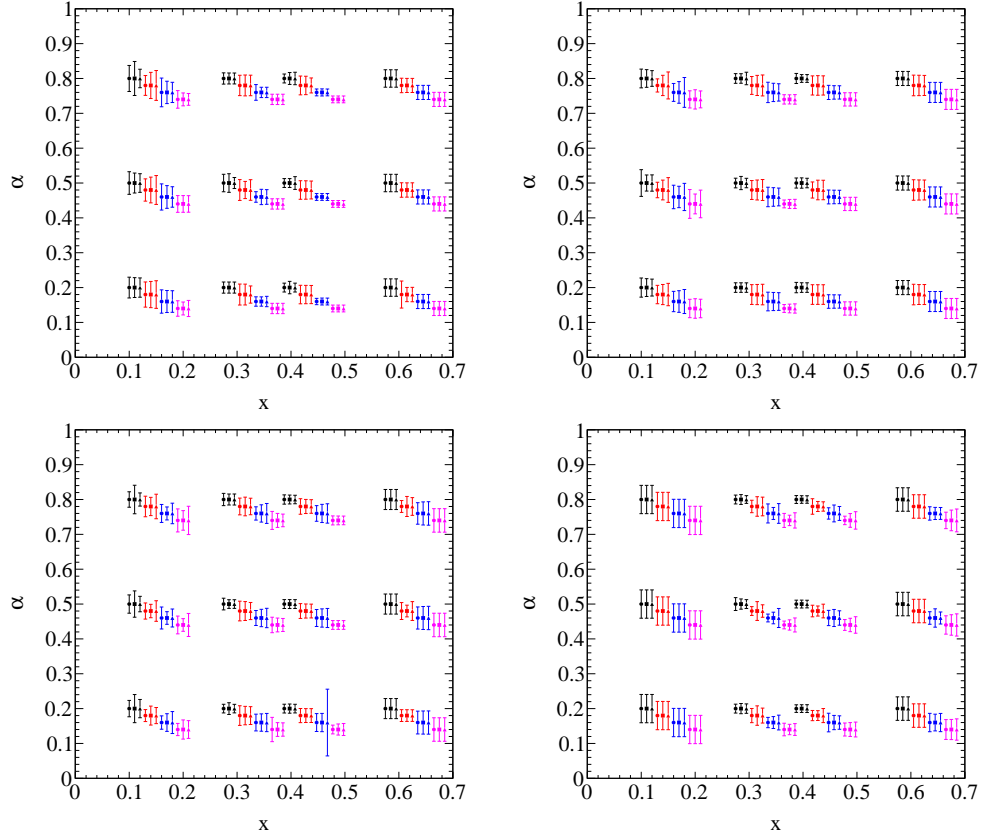


Figure B.8: Same as Fig. B.7 except for p-DVCS on a ^4He target.

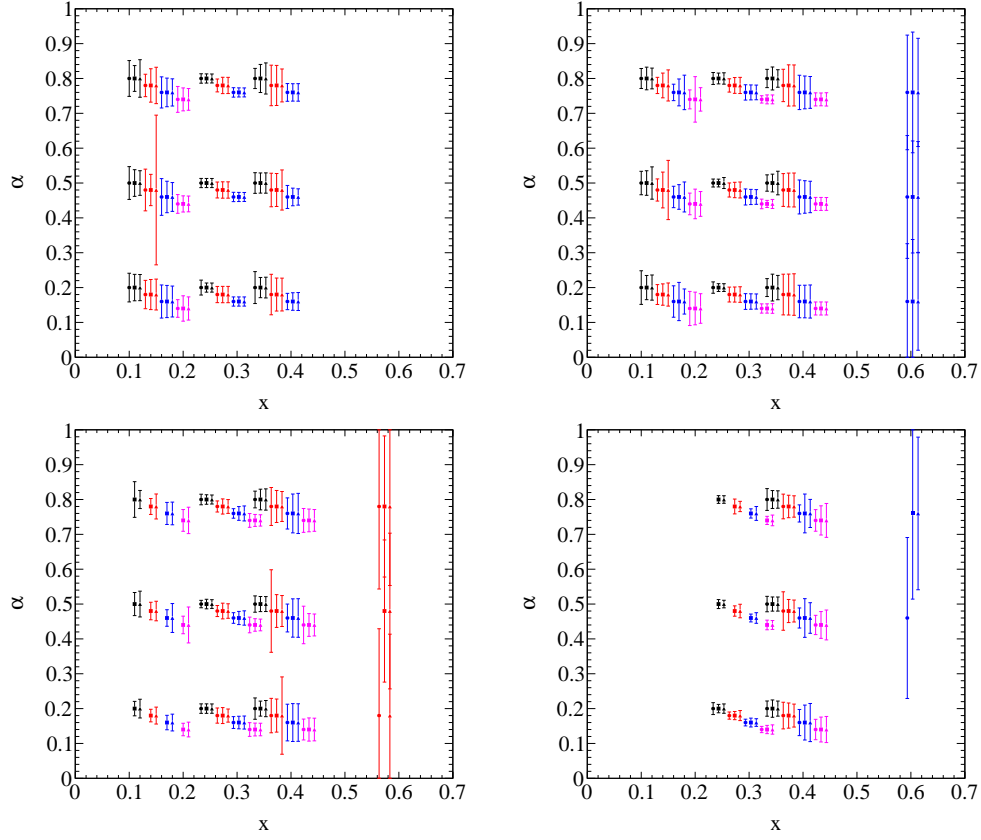


Figure B.9: Same as Fig. B.7 except for n-DVCS on a ^2H target.

B.2.1 Off-forward EMC Effect Ratio

The projected statistical uncertainties for the off-forward EMC ratio, defined in Equation 4.2, is shown in Fig. B.10.

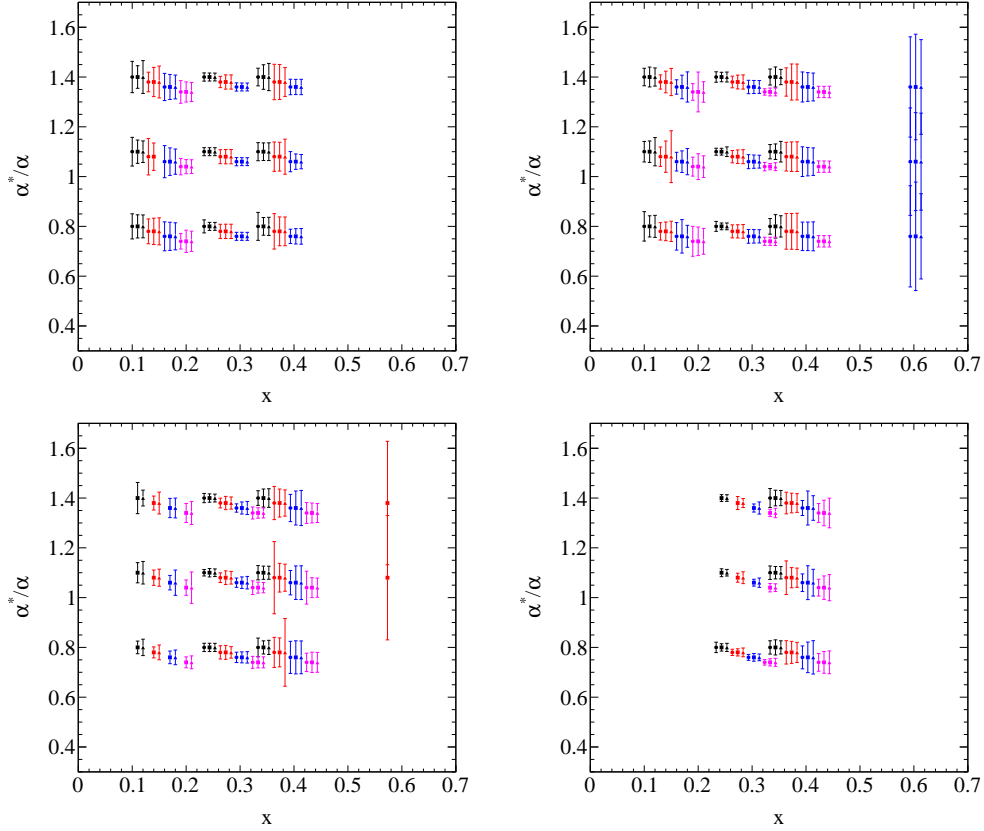


Figure B.10: The off-forward EMC ratio for a bound neutron to a quasi-free neutron (see Equation 4.2) for the same kinematics and binning described in Fig. B.9